Article:
Woolley, RM, Fairweather, M, Wareing, CJ et al. (15 more authors) (2014) An integrated, multi-scale modelling approach for the simulation of multiphase dispersion from accidental CO2 pipeline releases in realistic terrain. International Journal of Greenhouse Gas Control, 27. 221 - 238. ISSN 1750-5836

https://doi.org/10.1016/j.ijggc.2014.06.001

An Integrated, Multi-scale Modelling Approach for the Simulation of Multiphase Dispersion from Accidental CO_2 Pipeline Releases in Realistic Terrain

R.M. Woolley[a], M. Fairweather[b], and C.J. Wareing[c],
[abc]Institute of Particle Science and Engineering,
School of Process, Environmental and Materials Engineering,
University of Leeds, Leeds LS2 9JT, UK.
[a]r.m.woolley@leeds.ac.uk
(corresponding author)
Tel: +44 (0) 113 343 2351
Fax: +44 (0) 113 343 2384
[b]m.fairweather@leeds.ac.uk
[c]c.j.wareing@leeds.ac.uk

C. Proust[e], J. Hebrard[f], and D. Jamois[g]
[efg]INERIS, Dept. PHDS,
Parc Technologique ALATA,
BP 2, 60550 Verneuil-en-Halatte, France.
[e]christophe.proust@ineris.fr
[f]jerome.hebrard@ineris.fr
[g]didier.jamois@ineris.fr

V.D. Narasimhamurthy[l], I.E. Storvik[m], and T. Skjold[n]
[l]GexCon AS,
P.O. Box 6015, Bergen Bedriftssenter,
NO-5892 Bergen, Norway.
[l]vagesh@gexcon.com
[m]idar@gexcon.com
[n]trygve@gexcon.com

S.A.E.G. Falle[d]
[d]School of Mathematics,
University of Leeds, Leeds LS2 9JT, UK.
[d]s.a.e.g.falle@leeds.ac.uk

S. Brown[h], H. Mahgerefteh[i], and S. Martynov[j]
[hij]Department of Chemical Engineering,
University College London,
London WC1E 7JE, UK.
[h]solomon.brown@ucl.ac.uk
[i]h.mahgerefteh@ucl.ac.uk
[j]s.martynov@ucl.ac.uk

S.E. Gant[k]
[k]Health & Safety Laboratory,
Harpur Hill,
Buxton SK17 9JN, UK.
[k]Simon.Gant@hsl.gsi.gov.uk

D.M. Tsangaris[o], I.G. Economou[p*], G.C. Boulougouris[q], and N.I. Diamantonis[r]
[opqr]National Center for Scientific Research "Demokritos", Institute of Physical Chemistry, Molecular Thermodynamics and Modelling of Materials Laboratory,
GR–153 10 Aghia Paraskevi Attikis,
Greece.
[o]dtsangaris@chem.demokritos.gr
[p]economou@chem.demokritos.gr
[q]gboul@chem.demokritos.gr
[r]nidiama@chem.demokritos.gr
*Current address: Chemical Engineering Program, Texas A&M University at Qatar, PO Box 23874, Doha, Qatar

Submission of a full-length article to the International Journal of Greenhouse Gas Control, of unpublished material not submitted for publication elsewhere

Running title: Integrated Modelling of Accidental CO_2 Releases

ABSTRACT

The deployment of a complete carbon capture and storage chain requires a focus upon the hazards posed by the operation of pipelines transporting carbon dioxide (CO_2) at high pressure in a dense-phase (supercritical or liquid state). The consequences of an intentional or accidental release from such pipelines must be considered as an integral part of the design process. There are a number of unique challenges to modelling these releases due to the unusual phase-transition behaviour of CO_2. Additionally, few experimental observations of large-scale CO_2 releases have been made, and the physics and thermochemistry involved are not fully understood. This work provides an overview of elements of the EC FP7 CO2PipeHaz project, whose overall aim is to address these important and pressing issues, and to develop and validate mathematical models for multiphase discharge and dispersion from CO_2 pipelines. These are demonstrated here upon a full-scale pipeline release scenario, in which dense-phase CO_2 is released from a full-bore 36-inch pipeline rupture into a crater, and the resulting multiphase CO_2 plume disperses over complex terrain, featuring hills and valleys. This demonstration case is specifically designed to illustrate the integration of different models for the pipeline outflow, near-field and far-field dispersion.

KEYWORDS

CCS, CO_2, multi-phase flow, experimental measurement, mathematical modelling, pipeline depressurisation

1. INTRODUCTION

Carbon capture and storage (CCS) is a set of technologies designed to reduce CO_2 emissions from large point-sources of production such as coal-fired power stations and other industrial facilities. It involves the capture of CO_2 and its storage in suitable semi-permanent reservoirs such as naturally formed saline aquifers or depleted oil wells, instead of allowing its release to the atmosphere where it contributes to climate change. In most of the planned CCS projects, the CO_2 is transported from the capture to the storage sites in high-pressure pipelines, typically operating at pressures above 80 bar, where the CO_2 is in either a supercritical or liquid state, depending upon whether it is above or below the critical temperature of 304.19 K.

Whilst the physics of high-pressure releases of substances such as natural gas and propane is relatively well understood (Cowley and Tam, 1988; Richardson and Saville, 1996), CO_2 possesses some unusual physical properties which make its release behaviour more challenging to predict. As pure CO_2, its triple-point pressure and temperature are 5.18 bar and 216.55 K respectively, and at atmospheric pressure CO_2 exists in either a solid or gaseous state, with a sublimation temperature of 194.25 K. This means that there is likely to be complex phase-transition when CO_2 decompresses from an initial dense-phase state in the pipeline (i.e. as a supercritical or liquid fluid) into a solid and gaseous state at atmospheric pressure. The work undertaken in the EC FP7 CO2PipeHaz project (2009) has been pivotal to improving the understanding of this complex phase-transition behaviour and providing more accurate predictions of the consequence associated with CO_2 pipeline releases.

CO_2 is a colourless and odourless gas under ambient conditions, and is toxic if inhaled in air at concentrations around 5%, and likely to be fatal at concentrations of around 10% (NIOSH, 1996). Liquid CO_2 has a density approximately 50% less than that of water, but has a viscosity of magnitude more frequently associated with gases, and this property makes the transport of CO_2 an economically viable and attractive proposition. However, preliminary calculations and experimental evidence indicate that, due to it possessing a relatively high Joule-Thomson expansion coefficient, the rapid expansion of an accidental liquid release may reach temperatures below 180 K. Due to this effect, solid formation following a pipeline puncture or rupture is to be expected, and subsequently, at atmospheric pressure, the solid CO_2 will sublime into gas. In assessing the hazards posed by releases of CO_2, it is important to take account of the fact that the CO_2 gas will be much denser than air, due to both its

higher molecular weight and very low temperature. This could lead to a gravity-driven flow of high CO_2-concentration gas, which would tend to flow down slopes and accumulate in low-lying areas.

The modelling of outflow and subsequent atmospheric dispersion following pipeline failure is especially challenging given the large number of complex and often interacting processes governing the phenomena involved. The rupture of the pipeline results in a series of expansion waves that propagate into the undisturbed fluid in the pipe towards the intact end of the pipeline. These waves result in the acceleration of the fluid particles in the opposite direction and hence outflow. The precise tracking of these expansion waves and their propagation as a function of time and distance along the pipeline is necessary for the accurate prediction of the outflow, as well as any propagating fractures within the pipeline material. This involves detailed consideration of several processes including heat and mass transfer, unsteady fluid flow and thermodynamics (Mahgerefteh et al., 2012a). Additionally, given that the transportation of CO_2 will undoubtedly occur at high pressure, this means that the near-isentropic expansion resulting from a pipeline failure will likely induce two-phase flow. The modelling of the subsequent dispersion of CO_2 in the atmosphere also poses a number of difficulties due to the complex interaction of a number of physical and thermodynamic phenomena including the formation of stationary shock-cell structures, phase transition, and the behaviour of multi-phase systems. In the case of a full-bore rupture, this will inevitably occur within the confines of a crater excavated by the high-pressure release and the geometry of this crater will invariably affect the near-field dispersion of the release. Hence, this must be considered if suitable source terms are to be provided to the far-field dispersion models. Finally, the far-field atmospheric dispersion phenomena can only truly be understood if the fluid dynamics of the release are evaluated using a realistic terrain in which the effects of gravitational acceleration, buoyancy, wind, turbulence, and the behaviour of the different phases are considered.

This paper describes the development of novel multi-phase pipeline discharge and dispersion models applicable to dense-phase CO_2 pipelines, and their validation against recently obtained experimental data. The accidental release considered was of pure CO_2, initially at 150 bar and 283 K, from a pipeline 217 km in length and with an internal diameter of 0.914 m (36 inches). A full-bore guillotine rupture was modelled, which was assumed to take place 84 km from the feed-end of the pipeline. Terrain data obtained from the UK Ordnance Survey database (2013) was incorporated into the modelling to represent a realistic release scenario.

2. VALIDATORY EXPERIMENTAL WORK

Although it is clearly not possible to validate the overall model which integrates pipe-flow, pipe-release, near-field and far-field dispersion modelling, the accuracy of certain elements of the models was assessed against large-scale data acquired as part of the project.

Figure 1 shows a schematic of the rig and the sensor arrays used at INERIS for the experimental studies of large-scale CO_2 releases. The rig was used to acquire data regarding mass flow-rates, and near-field temperature and concentration distributions in a number of different release scenarios of varying nozzle sizes and initial pressures. These data have been used in the validation of the in-pipe, near-field, and far-field dispersion models, and further details can be found in the literature (Jamois et al., 2013). Part of this validation is discussed below, but further information be found in recent CO2PipeHaz project reports (Fairweather et al., 2011; Martynov, 2013; Narasimhamurthy et al., 2013).

In the flow field, the instrumentation consisted of twenty-six, radially distributed thermocouples, and six oxygen depletion sensors distributed along the centre-line axis of the jet. The region used for the near-field dispersion-model validation extended to 5 m from the release plane. This choice of the modelling domain size was due to the near-field model developments in this paper being concerned with the accurate representation of under-expanded, shock-laden, multi-phase jets, and the structure of their initial expansion to atmospheric conditions. By 5 m downstream of the release point, the jet has become self-similar in its properties, and has been at atmospheric pressure for a considerable distance. Hence, the modelling of the far-field region does not require such specialist treatment.

Figure 2 is a schematic of the release vessel, supported by photographs of the assembly including the release valve, stop valves, and the discharge orifice. The 2 m^3 spherical pressure vessel was thermally insulated, and can contain up to 1000 kg of CO_2 at a maximum operating pressure and temperature of 200 bar and 473 K, respectively. It is equipped internally with 6 thermocouples and 2 high-precision pressure gauges, and was connected to a discharge line of 50 mm inner diameter, with no internal restrictions. In total, the line is 9 m long including a bend inside the vessel, plunging to the bottom in order to ensure that it was fully submersed in liquid CO_2. Three ball valves were installed in the pipe. Two were positioned close to the vessel and the third near to the orifice holder. The first valve closest to the sphere was a manual safety valve, and the two others were remotely actuated. All valves were full-bore ball valves, sized appropriately for the pipe section.

The vessel was supported by four Mettler 0745 A load cells, enabling a continuous measurement of the CO_2 content with an uncertainty of plus or minus 0.5 kg. The determination of the mass flow-rate was performed within an accuracy of approximately 10%, mainly due to the noise present in the measurement signal during the release. These obtained measurements have been used to assist in the validation of the pipe out-flow models. In the sphere, the pressure was measured using a Piezoresistive type KISTLER 4045 A 200 sensor with a range of 0 to 200 bar and an accuracy of plus or minus 0.1%. This sensor was mounted directly to the flange of the sphere, as shown in Figure 3. Another Piezoresistive type KISTLER 4045 A 500 sensor, with a range of 0 to 500 bar, was connected to the sphere and served as a backup. The internal temperature of the vessel was measured at 6 points on the vertical axis of the sphere using 1mm sheathed, type K thermocouples, with an accuracy of plus or minus 0.25 K. Temperature immediately upstream of the orifice was similarly measured. The static pressure immediately upstream from the orifice was measured using a KULITE 0-350 bar instrument with an accuracy of ±0.5%. The vessel instrumentation is shown in Figure 3.

Various orifices were used at the exit plane of the discharge pipe, which were drilled into a large screwed flange. Figure 4 is a schematic of such, where the thickness of this flange (E) is 9 mm for the 6mm orifice and 15 mm for the 25 mm orifice. The diameter of the orifice (Φ) is constant over a length of 5 mm or 10 mm (e) and then expands with an angle of 45° towards the exterior.

3. IN-PIPE AND RELEASE-CONDITION MODELLING

3.1 Modelling Approach

To date, the majority of the pipeline outflow models reported in the literature have utilised the homogeneous equilibrium model (HEM) (Mahgerefteh et al., 1999; Mahgerefteh and Wong, 1999; Popescu, 2009; Webber et al., 1999) where the constituent fluid phases are assumed to remain in thermal and mechanical equilibrium during the decompression process. In contrast to the HEM, the homogeneous relaxation model (HRM) accounts for the delay in vaporisation during the decompression process using an empirical relaxation equation for the mass fraction of vapour phase, while assuming that the constituent phases are in mechanical equilibrium, i.e. that they move at the same velocity. In the HRM, the mass, momentum, energy and vapour quality conservation equations are respectively given by (Brown et al., 2013):

$$\frac{\partial \rho}{\partial t}+\frac{\partial}{\partial x}(\rho u)=0 \tag{1}$$

$$\frac{\partial}{\partial t}(\rho u)+\frac{\partial}{\partial x}\left(\rho u^2+p\right)=-\frac{f_w \rho u^2}{d} \tag{2}$$

$$\frac{\partial}{\partial t}(\rho E)+\frac{\partial}{\partial x}\left(u\left(E+p\right)\right)= \quad u\frac{f_w \rho u^2}{d} \tag{3}$$

$$\frac{\partial}{\partial t}(\rho \alpha)+\frac{\partial}{\partial x}(\rho u \alpha)=\rho\frac{\alpha_{eq}-\alpha}{\tau} \tag{4}$$

where ρ, u, p, d, f_w, α, and τ are respectively the mixture density, velocity, pressure, pipeline diameter, Fanning friction factor calculated using Chen's correlation (Chen, 1979), the dynamic vapour quality and a relaxation time accounting for the delay in the phase change transition as functions of time, t, and space, x. E represents the total mixture energy defined as:

$$E=\rho\left(e+\frac{1}{2}u^2\right) \tag{5}$$

where e is specific internal energy of the mixture:

$$e=\alpha e_{sv}(p)+(1-\alpha)e_{ml} \tag{6}$$

and ρ is the mixture density given by:

$$\frac{1}{\rho} = \frac{\alpha}{\rho_{sv}(p)} + \frac{(1-\alpha)}{\rho_{ml}(p, e_{ml})} \tag{7}$$

In equations (6) and (7), the subscripts *sv* and *ml* respectively refer to the saturated vapour and meta-stable liquid phases, which may be at different temperatures.

Based on experimental data on steady flow of CO_2 through a nozzle, the following correlation for the relaxation time τ was proposed (Angielczyk et al., 2010):

$$\tau = 2.15\times10^{-7}\left(\alpha\frac{\rho}{\rho_{sv}}\right)^{-0.54}\left(\frac{p_s(T_{in})-p}{p_c-p_s(T_{in})}\right)^{-1.76} \tag{8}$$

where, T_{in} is the feed temperature. ρ, p, p_c, ρ_{sv} and p_s are respectively the mixture density, fluid pressure, critical pressure, saturated vapour density at the given pressure and the saturation pressure at the given temperature.

In order to close the above model, an equation of state is required to predict the phase equilibria and thermodynamic properties of CO_2. A number of common cubic equations of state, e.g. the Soave-Redlich-Kwong (SRK) (Soave, 1972) and the Peng-Robinson (PR) (Peng and Robinson, 1976) equations of state were employed for this purpose in modelling pipeline decompression (Mahgerefteh et al., 2012a; Mahgerefteh et al., 2012b; Munkejord et al., 2010). However, given the importance of accurate predictions of the thermodynamic properties, a highly accurate thermodynamic model based on the Perturbed Chain-Statistical Associating Fluid Theory (PC-SAFT) equation of state, described further below, was developed by NCSR Demokritos as part of the CO2PipeHaz project (Diamantonis and Economou, 2011). To investigate the impact of the choice of the equation of state in the modelling of the CO_2 releases considered in this work, the two cubic equations of state mentioned earlier and the PC-SAFT equation are used here in validation studies. This is conducted by the integration of the Physical Properties Library (PPL) software package incorporating the various equations of state, with the outflow model. This coupling is undertaken using an interface developed by the CO2PipeHaz partners at NCSR Demokritos, and further discussed in Section 4.

The HRM has recently been applied to the modelling of CO_2 discharge following full-bore rupture of pipelines (Brown et al., 2013) where it was shown to produce reasonable agreement in comparison with available experimental data. As a further validation, this model has been applied to predict outflow from pipelines with small diameter punctures. For modelling purposes, a pipeline with an orifice at the release end is considered as depicted in Figure 5.

Given that the model described by equations (1) to (4) can only be solved numerically, an operator splitting method is used (LeVeque, 2002). This method breaks the solution down into two steps: firstly the conservative left-hand-side of equations (1) to (4) are solved using an upwind, flux differencing scheme based on the Harten, Lax, van Leer (HLL) approximate Riemann solver (Harten et al., 1983). Secondly, this solution is updated by solving a system of ordinary differential equations incorporating the expressions on the right-hand-side of equations (1) to (4). Full details of the algorithm are described in Brown et al. (2013).

3.2 Validation, Results and Discussion

The model described above has been applied to the simulation of flow through the experimental apparatus described in Section 2. Table 1 summarises the conditions of two tests chosen for the model validation in the present work. As can be seen from this table, the tests were performed using release orifices of two different diameters and two different initial vessel pressures and temperatures. Given that the focus of this study was to replicate the steady release through a puncture in a pipeline, the vessel initial pressures were assumed to be constant and simulations were run until a steady release rate was obtained.

Table 2 shows the mass flow rate, pressure drop from the reservoir, temperature and density of the CO_2 fluid at the release orifice, as predicted by the outflow model using the PR, SRK and PC-SAFT equations of state respectively for Test 2, as well as the measured mass flow rate. It can be seen that the results obtained using the PR equation are the most conforming with experimental observation with respect to prediction of the mass flow rate, while both the SRK and PC-SAFT equations slightly under-predict the experimental values. Similarly, a lower release pressure is obtained with the PR as compared to the SRK and PC-SAFT equations, while the SRK predicts a markedly lower density. Interestingly, all predictions

indicate that the CO_2 remains liquid within the pipe section, with flashing subsequently occurring at the orifice.

Table 3 shows both the predicted release properties and the measured data for Test 8. In this case only the PR and SRK equations were used as the larger diameter caused stability problems when using the PC-SAFT equation of state. Similarly to the discussion in respect to the predictions and data presented in Table 2, the PR equation of state gives the best agreement with experimental data, although it does slightly over-predict the measured mass flow-rate.

3.3 Hypothetical Pipeline Release with Realistic Terrain

The hypothetical case considered involved the full-bore guillotine rupture at 84 km from the feed end of a 914.4 m (36 inch) internal diameter, 217 km pipeline transporting pure CO_2 at 150 bar and 283 K. Along the pipeline length there were assumed to be two emergency shutdown valves placed at 23 km and 127 km from the feed end of the pipeline respectively, which are activated at 800s following the failure at a rate of 2.56 cm s^{-1}. Furthermore, the simplifying assumption was made that prior to the release the CO_2 fluid was stagnant in the pipeline. In simulations the closed-end boundary conditions were applied at both ends of the pipeline. It should be noted that the due to the length of the pipeline and the closure time of the valves used, the interaction of the flow with boundary conditions is expected to be minimal.

Two sets of outflow calculations were performed using the PR equation of state. The first case accounted for a realistic topography of the pipeline as shown in Figure 6, while in the second case a horizontal pipeline indicating a flat terrain was modelled. Figure 7 shows a comparative plot of the depressurisation history, in terms of the pressure at the release point, for both the cases studied for the upstream section of the pipeline. As can be seen, the resulting outflow predictions are relatively insensitive to the differences in pipeline inclination. There are only minor differences in the release pressures predicted in the initial stages, although these differences become more significant towards the end of the simulation. Figure 8 shows the variation of predicted release pressure for the downstream section for both the above cases. Again, there is no significant difference in the pressure histories for both cases which indicates the insignificance of the inclinations on the release data. For both cases

the predicted release pressure is approximately 7 bar by the end of the simulation. Finally, Figure 9 shows the total predicted discharge rate variation, from both ends of the pipeline, plotted against time for both cases. The flow rate predicted for the two cases is coincidental over much of the simulation duration. This result indicates that for the given terrain, the variation of the pipeline inclination has a small effect on the release. This lack of impact is explained by the relatively small contribution of the hydrostatic head to the total pressure in the pipeline during the initial period of its depressurisation.

4. THERMODYNAMIC PROPERTY MODELLING

Accurate and efficient prediction of thermodynamic properties of pure CO_2 and its mixtures with non-condensable gases of interest to CCS is key to successful modelling of accidental CO_2 releases from pressurised transportation pipelines. The Physical Properties Library (PPL) (Tsangaris et al., 2013) developed by NCSR Demokritos encapsulates a variety of thermodynamic methods capable of predicting these properties as functions of temperature, pressure and composition. Existing models applicable to CO_2 transportation conditions have been recently reviewed by Diamantonis et al. (2013). The PPL can predict properties such as density, fugacity, enthalpy, and viscosity using empirical, semi-empirical and theoretical models available in the literature or recently developed for CO_2 within the scope of this work.

Thermodynamic models for pure components and mixtures are often based on pure component constants such as molecular weight, critical properties, or an acentric factor. The PPL has an internal database that stores these pure component values and model parameters, and hence physical properties of pure components such as liquid density, heat capacity, speed of sound, and Joule-Thompson coefficient can be calculated by a number of different models available in the literature. The PPL supports the most popular models available including equations of state and empirical equations. It also supports the prediction of CO_2 mixture properties using popular models. These include cubic equations of state such as Redlich-Kwong (RK), Soave-Redlich-Kwong, and Peng-Robinson, specialized equations of state such as GERG, and advanced equations of state such as SAFT, PC-SAFT, and tPC-PSAFT.

For CO_2 and CO_2 mixtures, the PPL can be used to obtain the following properties:

- Volumetric (density, compressibility)
- Energy related (enthalpy, entropy, heat capacity)
- Free energy (Gibbs, fugacity)
- Derivative (Joule-Thomson, speed of sound)
- Transport (viscosity, diffusivity, thermal conductivity)

and the equilibrium properties can be obtained using the following methods:

- Cubic equations of state (RK, SRK, PR)
- Specialized equations of state (GERG)

- Advanced equations of state (SAFT/PC-SAFT/tPC-PSAFT)
- Empirical and semi-empirical models

The end user can select the desired method of calculation and the physical property of interest through appropriate library ‘calls’ and ‘options’ as described in the published Advanced Programming Interface (Tsangaris et al., 2013).

4.1 SAFT and PC-SAFT Equations of State

The focus of this work has been the development of accurate thermodynamic models for pure CO_2 and its mixtures with non-condensable gases for the temperature range of interest, based upon the SAFT family of equations of state. These equations of state combine an increase in accuracy compared to the cubic methods, and a reduced computational overhead compared to specialized formulations such as GERG. A brief description of SAFT follows. It is written as a summation of residual Helmholtz free energy terms that occur due to different types of molecular interactions in the system under consideration. This can be expressed as:

$$A^R = \left(A^{hs} + A^{disp}\right) + A^{chain} + A^{assoc} \tag{9}$$

where:

$$\frac{A^{hs}}{RT} = \frac{4n - 3n^2}{(1-n)^2} \qquad \text{is the hard-sphere term (Carnaham-Starling)} \tag{10}$$

$$\frac{A^{disp}}{RT} = \sum_{i=1}^{4}\sum_{j=1}^{9} D_{ij}\left(\frac{u}{kT}\right)^i\left(\frac{n}{\tau}\right)^j \qquad \text{is the dispersion term (Adler equation)} \tag{11}$$

$$\frac{A^{chain}}{RT} = (1-m)\ln\frac{1-0.5n}{(1-n)^3} \qquad \text{is the chain term (Wertheim)} \tag{12}$$

$$\text{and} \qquad \frac{A^{assoc}}{RT} = \sum_{A=1}^{M}\left(\ln X^A - \frac{X^A}{2}\right) + \frac{1}{2}M \qquad \text{is the association term (Wertheim)} \tag{13}$$

$$\text{with} \qquad n = \tau\rho m v^o = \tau\rho m v^{oo}\left(1 - C\exp\left(-\frac{3u^o}{kT}\right)\right)^3 \tag{14}$$

$$\frac{u}{k}=\frac{u^{o}}{k}\left(1+\frac{e}{kT}\right) \tag{15}$$

$$X^{A}=\frac{1}{1+\sum_{B=1}^{M}\rho X^{B}\Delta^{\mathrm{AB}}} \tag{16}$$

$$\Delta^{\mathrm{AB}}=g(d)^{seg}\left[\exp\left(\frac{\varepsilon^{AB}}{kT}\right)-1\right]\left(\sigma^{3}\kappa^{AB}\right) \tag{17}$$

$$g(d)^{seg}\approx g(d)^{hs}=\frac{1-\frac{n}{2}}{(1-n)^{3}} \tag{18}$$

where X^{A} is the fraction of molecules that have not formed a hydrogen bond at position A, Δ^{AB} is a function describing the strength of the hydrogen bond that forms between points A of a molecule and the position B of another molecule, and $g(d)^{seg}$ is the radial distribution function of hard spheres. m is the number of spherical segments in a molecule, τ =0.74048, C =0.12, D_{ij} are the global constants of the Adler equation, v^{oo} the characteristic volume of a molecule segment, and M is the total number of positions on a molecule for hydrogen bond formation

The difference between the SAFT and PC-SAFT equations of state is the dispersion term, which for PC-SAFT is expressed as:

$$\frac{A^{disp}}{RT}=-2\pi\rho I_{1}(n,m)m^{2}\varepsilon\sigma^{3}-\pi\rho mC_{1}I_{2}(n,m)m^{2}\varepsilon^{2}\sigma^{3} \tag{19}$$

where $$C_{1}=\left(1+Z^{hs}+\rho\frac{\partial Z^{hc}}{\partial\rho}\right)^{-1} \tag{20}$$

$$I_{1}(n,m)=\sum_{i=0}^{6}a_{i}(m)n^{i} \qquad \text{and} \qquad I_{2}(n,m)=\sum_{i=0}^{6}b_{i}(m)n^{i} \tag{21}$$

while a_{i} and b_{i} are functions of the chain length given as:

$$a_{i}(m)=a_{0i}+\frac{m-1}{m}a_{1i}+\frac{m-1}{m}\frac{m-2}{m}a_{2i} \tag{22}$$

$$b_i(m) = b_{0i} + \frac{m-1}{m} b_{1i} + \frac{m-1}{m}\frac{m-2}{m} b_{2i} \tag{23}$$

and Z^{hs} is the compressibility factor of hard spheres. Figure 10 is a graphical depiction of the molecular elements of the method.

The parameters used in SAFT and PC-SAFT are three for normal compounds, and two more for associating. Also there is one binary mixture coefficient that is used to correlate data and calculations for mixtures. Pressure and chemical potential occur as analytical derivatives of the residual Helmholtz energy from the previous equation set.

In SAFT and PC-SAFT, the hard-sphere, chain, and association terms can be extended to mixtures using the standard methodology. Thus, mixing rules are only required for the dispersion term. A mixing rule for the segment number m is given by the expression:

$$m = \frac{1}{2}\sum_i \sum_j x_i x_j \left(m_i + m_j\right) \tag{24}$$

Also, a second mixing rule for the dispersion energy parameter u/k based on the van der Waals one-fluid theory can be used which is based on the expression:

$$\frac{u}{k} = \frac{\sum_i \sum_j x_i x_j m_i m_j \left(u/k\right)_{ij} \left(u^0\right)_{ij}}{\sum_i \sum_j x_i x_j m_i m_j \left(u^0\right)_{ij}}$$

where
$$\left(u^0\right)_{ij} = \left[\frac{1}{2}\left(\left(u^0\right)_{ii}^{1/3} + \left(u^0\right)_{jj}^{1/3}\right)\right]^3 \tag{25}$$

Another mixing rule, based on volume fractions, has also been proposed:

$$\frac{u}{k} = \frac{\sum_i \sum_j x_i x_j m_i m_j \left(u/k\right)_{ij} \left(u^0\right)_{ii} \left(u^0\right)_{jj}}{\sum_i \sum_j x_i x_j m_i m_j \left(u^0\right)_{ii} \left(u^0\right)_{jj}} \tag{26}$$

Both mixing rules are based on the assumption that the local and the bulk composition of the fluid are similar.

4.2 Validation, Results and Discussion

The PPL and especially the newly developed SAFT-based equation of state applicable to pure CO_2 and its mixtures was developed and tested within the scope of the CO2PipeHaz project. Direct comparison between SAFT predictions, experimental data and other classical equation of state predictions was used in the validation of the new equation. Validation included a variety of components, conditions and physical properties of interest to CCS.

Initially, the models were validated with respect to fluid phase equilibria (Diamantonis and Economou, 2012; Tsangaris et al., 2013), and binary and ternary mixtures of CO_2 with non-condensable gases were studied at pipeline transportation conditions. Subsequently, single phase volumetric, energy related, and the derivative properties were examined. The PPL calculates derivative property values analytically whenever possible. For some cases however, analytical differentiation of the equation of state is not possible and numerical differentiation is used instead. The derivative properties of interest to this work are the heat capacities (isobaric and isochoric), the speed of sound, the Joule-Thomson coefficient, the isothermal compressibility coefficient and the thermal expansion coefficient, as given in Table 4. These quantities can be derived from the equation of state and greatly affect the predictions of rate of pipeline depressurization during accidental release. As a result, accurate modelling is critical to hazard identification studies, and prediction and validation of the derivative properties has been documented (Diamantonis and Economou, 2011; Diamantonis et al., 2013). Finally, the newly proposed equation of state combined with existing semi-empirical transport-property models were validated for viscosity and the self-diffusion coefficient.

Figure 11 is a typical example of the improved capacity of the newly developed SAFT equation of state in the prediction of the isothermal compressibility of multi-component systems. Experimental data for derivative properties of complex mixtures are scarce in the literature. Amongst what is available (Alsiyabi et al., 2012), the CO_2-N_2-CH_4-H_2 system was selected due to it resembling candidate CO_2 pipeline mixtures better. Figure 11 compares predictions obtained from the Peng-Robinson and the newly developed PC-SAFT equations of state, and PC-SAFT displays a notably superior average absolute deviation error of 5.3 %

against 33.2 % for the classical approach. It should be emphasized that no tuning to isothermal compressibility data has been undertaken in the construction of any model. The improved capacity of PC-SAFT is attributed more to the fact that the mathematical terms resemble the physical interactions more closely, and less to the fact that PC-SAFT has slightly more complex functional form and an extra adjustable parameter.

5. NEAR-FIELD MULTI-PHASE DISPERSION MODELLING

5.1 Turbulent Flow Calculations

Predictions were based on the solutions of the Favre-averaged, density-weighted forms of the transport equations for mass, momentum, and total energy (internal energy plus kinetic energy), as described below by equations 27, 28, and 29 respectively:

$$\frac{\partial \overline{\rho}}{\partial t} + \frac{\partial}{\partial x_i}\left(\overline{\rho}\tilde{u}_i\right) = 0 \tag{27}$$

$$\frac{\partial}{\partial t}\left(\overline{\rho}\tilde{u}_i\right) + \frac{\partial}{\partial x_j}\left(\overline{\rho}\tilde{u}_i\tilde{u}_j + \overline{p} + \overline{\rho}\widetilde{u_i''u_j''}\right) - s_u = 0 \tag{28}$$

$$\frac{\partial \tilde{E}}{\partial t} + \frac{\partial}{\partial x_i}\left[(\tilde{E} + \overline{p})\tilde{u}_i - \tilde{u}_i\overline{\tau}_{ij}\right] - \frac{\partial}{\partial x_i}\left(\mu_t T \frac{\partial S}{\partial x_j}\right) - s_E = 0 \tag{29}$$

Representation of the Reynolds stresses ($\widetilde{u_i''u_j''}$), and hence the closure of this equation set, was achieved via the $k-\varepsilon$ turbulence model (Jones and Launder, 1972). Solutions of the time-dependent, axisymmetric forms of the descriptive equations were obtained using a modified version of an in-house general-purpose fluid dynamics code. Integration of the equations employed a second-order accurate, upwind, finite-volume scheme in which the transport equations were discretised following a conservative control-volume approach, with values of the dependent variables being stored at the computational cell centres. Approximation of the diffusion and source terms was undertaken using central differencing, and an HLL (Harten et al., 1983), second-order accurate variant of Godunov's method applied with respect to the convective and pressure fluxes. The fully-explicit, time-accurate method was a predictor-corrector procedure, where the predictor stage is spatially first-order, and used to provide an intermediate solution at the half-time between time-steps. This is then subsequently used at the corrector stage for the calculation of the second-order fluxes. A further explanation of this algorithm can be found elsewhere (Falle, 1991).

The calculations also employed an adaptive finite-volume grid algorithm which uses a three-dimensional rectangular mesh with grid adaption achieved by the successive overlaying of

refined layers of computational mesh. Figure 12 demonstrates this technique in a two-dimensional planar calculation of the near-field of a sonic CO_2 release. Where there are steep gradients of variable magnitudes such as at flow boundaries or discontinuities such as the Mach disc, the mesh is more refined than in areas such as the free stream of the surrounding fluid. The model to describe the fluid flow-field employed in this study was cast in an axisymmetric geometry for the validatory calculations of jet releases. A full three-dimensional scheme was applied to the crater calculations although the use of symmetry boundaries aided a reduction in computational expense. A full description of the equations solved is reported elsewhere (Wareing et al., 2013)

Although the standard k-ε model has been extensively used for the prediction of incompressible flows, its performance is well known to be poor in the prediction of their compressible counterparts. The model consistently over-predicts turbulence levels and hence mixing due to compressible flows displaying an enhancement of turbulence dissipation. A number of modifications to the standard k-ε model have been proposed by various authors, which include corrections to the constants in the turbulence energy dissipation rate equation (Baz, 1992; Chen and Kim, 1987), and to the dissipation rate itself (Sarkar et al., 1991; Zeman, 1990). Previous works by one of the present authors (Fairweather and Ranson, 2003, 2006) have indicated that for flows typical of those being studied here, the model proposed by Sarkar et al. (1991) provides the most reliable predictions. This model specifies the total dissipation as a function of a turbulent Mach number and was derived from the analysis of a direct numerical simulation of the exact equations for the transport of the Reynolds stresses in compressible flows. This approach was incorporated into the modelling described herein.

5.2 Non-ideal Equation of State

The Peng-Robinson equation of state (Peng and Robinson, 1976) is satisfactory for predicting the gas-phase properties of CO_2, but when compared to that of Span and Wagner (1996), it is not so for the condensed phase. Furthermore, it is not accurate for gas pressures below the triple point and, in common with any single equation, it does not account for the discontinuity in properties at the triple point. In particular, there is no latent heat of fusion.

Span and Wagner (1996) give a formula for the Helmholtz free energy that is valid for both the gas and liquid phases above the triple point, but it does not take account of experimental

data below the triple point, nor does it give the properties of the solid. In addition, the formula is too complicated to be used efficiently in a computational fluid dynamics code. A composite equation of state was therefore constructed to determine the phase equilibrium and transport properties for CO_2. The inviscid version of the overall model is presented in detail elsewhere (Wareing et al., 2013) and the method considered here is extended for the turbulent closure of the fluid-flow equations detailed in the previous section. In this, the gas phase is computed from the Peng-Robinson equation of state (Peng and Robinson, 1976), and the liquid phase and saturation pressure are calculated from tabulated data generated with the Span and Wagner (1996) equation of state and the best available source of thermodynamic data for CO_2, the Design Institute for Physical Properties (DIPPR) 801 database, access to which can be gained through the Knovel library (DIPPR, 2013). To calculate the solid density, the same approach as Witlox et al. (2009) is used, and expressed as:

$$\rho = 1289.45 + 1.8325T \; kg\, m^{-3} \tag{30}$$

again based on property information from the DIPPR 801 Database. From Liu (1984), the sound speed in solid CO_2 at atmospheric pressure and 296.35 K is 1600 m s^{-1} and it is assumed that this is independent of temperature and pressure. Note that the results given below are extremely insensitive to the solid density and sound speed. The saturation pressure above and below the triple point is taken from Span and Wagner (1996).

Figure 13 shows the predicted internal energy of the gas and condensed phases on the saturation line. The transition from liquid to solid was smoothed over 4 K with a hyperbolic tangent function centred on the triple point. This was done for computational reasons in order to ensure the function and its differentials are smooth.

Calculations of the thermodynamics in the pure CO_2 system indicated that in this case, little difference was observed between results obtained using the approach described above, and that presented in Section 4. Hence, for the unique case of a pure CO_2 release, the composite non-ideal equation of state was used in the form of look-up tables to increase computational efficiency. It will be essential to apply the more advanced equations of state such as PC-SAFT when considering systems containing mixtures of CO_2 with impurities.

5.3 Homogeneous Equilibrium and Relaxation Models

In an HEM, all phases are assumed to be in dynamic and thermodynamic equilibrium. *Id est* they all move at the same velocity and have the same temperature. In addition, the pressure of the CO_2 vapour is assumed to be equal to the saturation pressure whenever the condensed phase is present. The pressure of the condensed phase CO_2 is assumed to be equal to the combined pressure of CO_2 vapour and air (the total pressure).

The assumptions associated with the HEM are reasonable provided the CO_2 liquid droplets or solid particles are sufficiently small. There are some indications that this may not be true, in particular for test calculations in which the release is from a nozzle with a diameter of the order of centimetres. Hence, the model was further developed as an HRM, in that a relaxation time was introduced with respect to the transport of the dense phase. This has the effect of numerically representing the time taken for the dense phase to attain dynamic equilibrium with the fluid phase. Again, a full description of both the HEM and HRM can be found elsewhere (Woolley et al., 2013).

5.4 Code Validation against CO_2 Release Data

Figure 14 depicts centreline predictions of temperature and O_2 molar concentration plotted against experimental data for Test 2 at axial locations of 2, 3, 4, and 5 m. This test was undertaken using the 6 mm nozzle, and predictions can be seen to be in good agreement with observation. A slight over-prediction of temperature is observed in the very near-field, leading to a similarly slight under-prediction further downstream. However, predictions remain well within an acceptable range of experimental error. Again with reference to Figure 14, this over-prediction of temperature is translated into a slight over-prediction of O_2 concentration, at an axial location of 1 m.

In addition, Figure 15 shows predictions of radial temperature profiles plotted against experimental data for Test 8, performed by INERIS, at axial locations of 1, 2 and 5 m. The model qualitatively and quantitatively captures the thermodynamic structure of the sonic releases, and although there is a small discrepancy with the observed and predicted spreading rates in the very near-field, calculations lie within the accepted error range of the experimental data. Results obtained from calculations of two further tests, Tests 6 and 7 (not shown), were seen to be of a similar level of agreement to Test 8. Further discussion

regarding this validation exercise, and the results obtained, can be found in Woolley et al. (2013).

5.5 Crater Calculation Geometry and Sample Results

Figure 16 shows the chosen geometry of the crater formed after the pipeline guillotine rupture. This geometry was chosen, based upon incident data for natural gas pipelines taken from the literature (Kinsman and Lewis, 2002; McGillivray and Wilday, 2009).

This geometry was incorporated into a three-dimensional model for predicting the near-field dispersion characteristics, and Figure 17 shows an example of such a set-up in which one quarter of the crater has been modelled by applying appropriate symmetry boundaries. Figure 17 (a) depicts a cut along the centreline on the y-axis, which lies along the centre of the release pipe at x=0. The z dimension represents the crater depth, and symmetry boundaries are located at x=0 and y=15 m. Figure 17 (b) is looking down on to a plane in the x dimension, bisecting the pipe at a depth of 1.5 m. The symmetric left boundary at x=0 can also be seen to bisect the pipe. As previously mentioned, the uppermost boundary at y=15 m is also symmetric, and represents the companion jet release in a symmetrical full-bore release scenario.

Figure 18 shows sample predictions of a typical release obtained from the application of this crater geometry, with initial conditions (pressure, temperature, density, velocity, and phase composition) provided by the pipe outflow model described earlier. The flow is modelled as a steady state, using the predicted conditions at the pipeline orifice 30 seconds after the start of the release, following the methodology proposed for modelling transient pipeline releases by Carter (1991), and Bilio and Kinsman (1997). Dense-phase CO_2 mass fraction and total velocity predictions are presented, and the features of such a highly under-expanded jet can be seen, including the formation of a Mach disc, and the acceleration of the flow to supersonic velocities. Figure 19 and Figure 20 depict predictions of the full-bore release on a section located just above ground level and on a plane orthogonal to the z axis at 0.01 m. Figure 19 shows mixture fractions of total CO_2, solid CO_2, air, and gas, and overall density and temperature. Figure 20 shows the velocity components, total velocity, turbulence kinetic energy, and turbulence kinetic energy dissipation rate. To interface these results from the near-field model with the far-field dispersion models, described below as FLACS and

ANSYS-CFX, equivalent point-source boundary conditions were calculated by integrating the data shown in Figures 19 and 20 within an envelope defined by a CO_2 concentration of 0.1%. The resulting integrated source values are as given in Table 5.

These source terms were subsequently used for far-field dispersion calculations undertaken by partners HSL and GexCon AS, and reported upon in Section 6.

6. FAR-FIELD MULTI-PHASE DISPERSION MODELLING

Far-field modelling of the dispersion of two-phase (gaseous and particulate) CO_2 was undertaken using two different commercial computational fluid dynamic codes: FLACS (GexCon AS, 2013); and ANSYS-CFX (ANSYS, 2011). In both cases, the continuous gas-phase was solved in the Eulerian reference frame, while a Lagrangian formulation was used for the dispersed particle phase. In addition, both far-field models employed the same source boundary conditions, where the CO_2 jet conditions at the inlet plane were taken from the near-field dispersion model outputs, as described above, which consisted of integrated planar profiles of velocity, temperature, CO_2 solid and gas concentration, turbulence kinetic energy and turbulence dissipation rate. Distinct features of each of the individual codes are given below.

6.1 ANSYS-CFX

The CFX dispersion model for two-phase CO_2 releases used the Lagrangian particle-tracking model in ANSYS-CFX version 14 (ANSYS, 2011). The process of sublimation was simulated using the standard evaporation model, with suitable Antoine equation coefficients for solid CO_2 sublimation. Drag between the CO_2 particles and the surrounding gas phase was calculated using the drag model of Schiller and Naumann (1933) combined with the stochastic dispersion model of Gosman and Ioannides (1981) to account for turbulence effects. Heat transfer between the gaseous and solid phases was modelled using the Ranz-Marshall correlation (Ranz and Marshall, 1952) and turbulence effects in the gas phase were modelled using the Shear-Stress Transport (SST) model of Menter (1994).

To account for the effects of ambient humidity, the modelled gas phase was composed of a mixture of three components: dry air, CO_2, and water vapour, each of which was treated as an ideal gas. An additional dispersed-droplet Eulerian phase was used to account for condensed water droplets, which were assumed to have the same velocity as the surrounding gas phase. Source terms in the continuity and energy conservation equations were used to model the process of water vapour condensation and evaporation. Brown and Fletcher (2005)

previously demonstrated a similar approach to the modelling of atmospheric plumes from alumina refinery calciner stacks. It is useful to model humidity not only in terms of its effect on the dispersion behaviour, but also to provide predictions of condensed water droplet concentration, from which the plume visibility can be inferred. The visibility of the CO_2 plume has important practical implications for emergency planning and risk assessment.

The computational grids used with CFX in the present work were unstructured, using both tetrahedral and prism-shaped cells. Previous tests have shown that relatively fine grids are needed to resolve the sublimation process in two-phase CO_2 jets and therefore in excess of 3 million nodes were used in the CFX simulations presented here.

The near-field dispersion model outputs do not currently include predictions of the CO_2 particle size, which is an important input for the Lagrangian two-phase dispersion model. The size of the solid CO_2 particles produced by dense-phase CO_2 releases is uncertain, and it cannot be measured reliably in large-scale releases. However, previous work has shown that homogeneous equilibrium dispersion models provide reasonably good predictions of temperatures and concentrations in dense-phase CO_2 jets produced by orifices up to 50 mm in diameter (Dixon et al., 2012; Witlox et al., 2012). These models assume that the particles have the same temperature and velocity as the surrounding gas phase, which implies that the particles must be very small. Analysis of CO_2 particle sizes by Hulsbosch-Dam et al. (2012) has also suggested that their initial diameter once the jet has expanded to atmospheric pressure should be in the range 1-20 μm. In the present work the CO_2 particles are assigned an initial uniform diameter of 20 μm at the inlet plane, and their diameter subsequently reduces as they sublimate.

At the far-field boundaries, logarithmic wind velocity profiles and turbulence levels were specified using the approach described by Richards and Hoxey (1993). For the thermal boundary conditions, it is assumed that the stability of the atmospheric boundary layer is neutral.

Further information on the CFX dispersion model for two-phase CO_2 releases can be found in the work of Dixon et al. (2012).

6.2 FLACS

In the current study, two-phase CO_2 dispersion phenomena in FLACS (GexCon AS, 2013) are modelled using an Euler-Lagrangian method (Ichard, 2012). The numerical particles are modelled as point-particles (Loth, 2000), with the particles considered incompressible, non-reacting, and spherical in shape. Particle sizes are further represented by a uniform distribution. The governing equations solved for the continuous gas phase are the compressible form of Reynolds-averaged Navier-Stokes equations, where turbulence is modelled using a standard k-ε model (Launder and Spalding, 1974). A two-way coupling between the continuous gas-phase and the dispersed particle-phase is established through source terms in the mass, momentum, and energy equations (Peirano et al., 2006). In addition, particle-turbulence interaction is accounted for by special source terms in the turbulence kinetic energy and the dissipation rate of turbulence kinetic energy equations (Mandø et al., 2009).

A simplified form of the original equation of Maxey and Riley (1983) is used for the particle momentum equation, where the simplification is based on the analysis of Armenio and Fiorotto (2001) for a wide range of particle-fluid density ratios. In the present particle momentum equation, both the buoyancy force and the drag force were considered, while the added-mass force and the Basset history force were ignored since they are negligibly small when compared to the drag force (Armenio and Fiorotto, 2001). In addition, the pressure-gradient force term was also omitted, since its influence is small in large particle-fluid density ratio problems (Armenio and Fiorotto, 2001). The instantaneous fluid velocity seen by the particle, which is an unknown parameter in the particle momentum equation, is modelled through stochastic differential equations. A modified Langevin equation derived by Minier and Peirano (2001) was used for this purpose.

Particle deposition and interaction with obstacles was modelled (Crowe, 2005), while particle-particle interactions such as collisions, breakup and coalescence were not taken into account. In addition, humidity effects were not considered in the present version of the Lagrangian particle-tracking model.

The governing equations were solved on a staggered Cartesian grid using a finite-volume method. The solver for both the continuous phase and the dispersed phase was second-order accurate. A central-differencing scheme is used for the diffusive fluxes, while a hybrid scheme with weighting between upwind and central-differences was employed for the convective fluxes. Time-marching was carried out using an implicit backward-Euler scheme

and the discretized equations were solved using a BICGStab iterative method with the SIMPLE pressure correction algorithm (Versteeg and Malalasekera, 2007). Readers are referred to Ichard (2012) for further information concerning FLACS Lagrangian particle-tracking model and its validation.

6.3 Implementation of Realistic Terrain and Boundary Conditions

The realistic terrain employed was obtained from UK Ordnance Survey data and incorporated into the FLACS and CFX models, as shown in Figure 21. The length and width of the domain size in each case is 10 km and 5 km respectively. The FLACS domain extended to a height of approximately 1 km, whilst a lesser height was used in CFX, which varied from 260 m to 610 m depending upon the location. The computational grids used in the two codes were very different as FLACS employed a multi-block Cartesian mesh with 2.7 million grid points, whilst CFX used an unstructured grid of 3.2 million nodes that was composed of mainly tetrahedral cells, with prism-shaped cells along the solid boundaries.

For the dispersion model boundary conditions, the CO_2 source from the crater was specified using the conditions given in Table 5. For the turbulence source conditions in FLACS, a relative turbulence intensity of 0.1985 and turbulence length scale of 0.034 m, obtained from averaged k and ε values in Figure 20, were used. In both the FLACS and CFX models, the CO_2 particles were assigned an initial uniform diameter of 300 µm and 20 µm, respectively. The likely size of particles produced in dense-phase CO_2 releases is largely unknown, certainly for releases of the scale considered here, as discussed earlier. In addition, the initial temperature of the CO_2 particles in the FLACS simulation was set to the sublimation temperature of 194.25 K. For the upwind boundary condition, logarithmic cross-wind velocity profiles were used with a reference speed of 2 m s^{-1} for the FLACS simulations and 5 m s^{-1} for the CFX simulations, at a reference height of 10 m. Both models assumed Pasquill class type D (neutral) atmospheric stability and a ground roughness of 0.1 m, suitable for rural roughness with low crops and occasional large obstacles. The ambient temperature was 283 K, and for a maximum depressurisation time of 200 seconds, the total mass discharge predicted by the pipeline outflow model was approximately 2700 tonnes. Therefore, with reference to the mass flow rate in Table 5, the release duration was approximately 138 seconds, and the FLACS simulations were performed for a release over this period using a

transient solver. Following the release cut-off, the dispersion calculations were simulated for a further 400 seconds. In contrast, the CFX simulations were performed using a steady solver, and the results therefore provide predictions assuming that the release was prolonged.

6.4 Results and Discussion

The predicted CO_2 jet in the vicinity of the crater is shown in Figure 22 for the FLACS and CFX models. Owing to the smaller particle-size used in the CFX simulations, it was found that all of the particles sublimated within the airborne jet, and these particle trajectories are shown in the right-hand plot of Figure 22. In contrast, the larger initial particle-size prescribed in the FLACS simulations resulted in some solid-CO_2 mass raining-out on to the terrain. Towards the end of the FLACS simulation, it was recorded that approximately 20% of the total mass discharged, at around 550 tonnes, had rained-out on the ground. This result suggests that banks of solid CO_2 might be formed in CO_2 pipeline releases if particles with diameters of the order 300 µm or larger are produced in the jet leaving the crater.

Figure 23 shows the steady-state cloud predicted by the CFX model. These predictions are shown using three different CO_2 mean concentration levels to define the edge of the cloud: 1%, 2% and 4% v/v. For these three cases, the cloud extends to approximately 5 km, 4 km, and 2 km respectively. At low concentrations of 1% or 2%, CO_2 is considered not harmful but these concentrations may correlate to the extent of the visible cloud due to condensed water vapour (i.e. mist). A concentration of 4% v/v CO_2 corresponds to the Immediately Dangerous to Life and Health (IDLH) value recommended by NIOSH (1996). The CFX results show that even with a wind speed of 5 m s^{-1}, the presence of the terrain has a large effect on the dispersion of the CO_2 cloud, and rather than being blown downwind, the cloud spreads mostly in the lateral directions, up and down the valley.

Figure 24 shows the CO_2 cloud predicted by FLACS at various intervals in time. These are after the beginning of the release, a little after the release cut-off, 100 seconds after the release cut-off, and finally near the end of the simulation. Owing to the finite total mass discharge, the CO_2 cloud is notably smaller than that predicted by the steady-state release CFX simulations. It can be observed from Figure 24(b) that the maximum CO_2 concentration almost reduces to half (45% v/v) a little after the release cut-off and gradually reduces with time to reach 4% v/v near the end of the simulation (Figure 24(d)).

7. CONCLUSIONS

The process of simulating a hypothetical ‘realistic’ release from a buried 0.914 m (36 inch) diameter, 217 km long pipeline has been demonstrated. Models for the pipeline outflow, near-field and far-field dispersion have been integrated, along with suitable thermophysical property models. A schematic representation of this integration is given as Figure 25. Results from the outflow model have been used to specify inlet boundary conditions for the near-field dispersion model, which in turn has provided inlet boundary conditions for the far-field dispersion model. Where possible, the models have been validated against data available in the open literature, and also using data generated by partners during the execution of the EC FP7 CO2PipeHaz project.

The work has demonstrated that it is feasible, in principle, to simulate such industrially-relevant flows. However, the computing resources required were found to be significant, requiring of the order weeks of computing time for the full solution. The use of this type of integrated modelling approach therefore appears unlikely to become widespread for routine CO_2 pipeline risk assessment at present, if conducted upon standard workstation computers. However, these models should be immediately useful for the investigation of particular aspects of risk assessments. For instance, those where there are large differences in terrain heights close to a pipeline route, and where the effect of the terrain on the dispersion behaviour needs to be assessed in detail.

One of the limitations of the approach demonstrated here is that the models are integrated in a linear fashion, with no feedback between them. This feedback could be particularly important if low wind speeds were to be simulated. In the present near-field model, the flow entrained into the crater was assumed to consist of ambient air, whereas under low wind-speed conditions, the CO_2 jet may fall to the ground near the crater and this flow could include very high CO_2 concentrations. The two-way coupling of the near- and far-field dispersion models is not trivial, but it should be reasonably straightforward to apply the concentrations predicted by the far-field model onto the near-field model boundaries, and for this process to be iterated a number of times if required, to account for these effects.

In the future, it would be useful to further validate this integrated modelling approach against publicly-available datasets, particularly those involving releases of dense-phase CO_2 from buried pipelines. The present work has demonstrated that the size of the solid CO_2 particles

released from a crater can have a significant effect upon the dispersion characteristics of the release.

In view of the fact that most routine pipeline risk assessments will be carried out using integral or other phenomenological models that assume dispersion over flat terrain, it would be useful to use the models demonstrated here to determine under what set of conditions such models might provide unreliable results. It should be possible to investigate this matter by varying inputs (e.g. pipeline release rate, wind speed, terrain height differences) to the type of models presented here to investigate under what combination of conditions the results deviate significantly from those of more pragmatic modelling approaches.

Finally, from an emergency-planning perspective, it would be useful to further develop and validate models that are able to predict the extent of the visible CO_2 plume, as well as its extent in terms of its instantaneous hazardous CO_2 concentrations. Under typical humid northern European climatic conditions, a full-bore pipeline rupture may produce an optically-dense cloud that extends many kilometres.

8. NOMENCLATURE

Roman letters:

A	Helmholtz free energy
d	diameter
e	internal energy
E	total energy
f_w	Fanning friction factor
p	pressure
s	source term
T	temperature
t	time
u	velocity
v	volume
x	spatial location

Superscripts:

$\overline{A}$	Reynolds average
$\tilde{A}$	Favre average
A''	fluctuating component

Greek letters:

α	dynamic vapour quality
ρ	density
τ	relaxation time
τ_{ij}	shear stress

Subscripts:

c	critical
eq	equilibrium
i	spatial indice
in	inlet
j	spatial indice
ml	meta-stable liquid
s	at saturation
sv	saturated vapour
t	turbulent

9. ACKNOWLEDGEMENTS

The research leading to the results described in this paper has received funding from the European Union 7th Framework Programme FP7-ENERGY-2009-1 under grant agreement number 241346. The paper reflects only the authors' views and the European Union is not liable for any use that may be made of the information contained herein.

One of the authors, S.E. Gant (HSL), was additionally funded by the UK Health and Safety Executive. The contents of this paper, including any opinions and/or conclusions expressed, are those of the authors alone and do not necessarily reflect HSE policy.

10. REFERENCES

Alsiyabi, I., Chapoy, A., Tohidi, B., 2012. Effects of impurities on speed of sound and isothermal compressibility of CO_2-rich systems, 3rd International Forum on the Transportation of CO_2 by Pipeline, Gateshead, UK.

Angielczyk, W., Bartosiewicz, Y., Butrymowicz, D., Seynhaeve, J.-M., 2010. 1-D Modeling Of Supersonic Carbon Dioxide Two-Phase Flow Through Ejector Motive Nozzle, International Refrigeration and Air Conditioning Conference. 12-15 July, Purdue University, Lafayette, USA, p. 2362.

ANSYS, 2011. ANSYS CFX-Solver Theory Guide - Release 14.0.

Armenio, V., Fiorotto, V., 2001. The Importance of the Forces Acting on Particles in Turbulent Flows. Phys. Fluids 13(8), 2437-2440.

Baz, A.M.E., 1992. Modelling Compressibility Effects on Free Turbulent Shear Flows, 5th Biennial Colloquium on Computational Fluid Dynamics, UMIST.

Bilio, M., Kinsman, P., 1997. MISHAP - HSE's pipeline risk assessment methodology. Pipes and Pipelines International July-August, 5-12.

Brown, G.J., Fletcher, D.F., 2005. CFD Prediction of Odour Dispersion and Plume Visibility for Alumina Refinery Calciner Stacks. Process Saf. Environ. 83(B3), 231-241.

Brown, S., Martynov, S., Mahgerefteh, H., Proust, C., 2013. A Homogeneous Equilibrium Relaxation Flow Model for the Full Bore Rupture of Dense Phase CO_2 Pipelines. Int. J. Greenh. Gas Con. 17, 349-356.

Carter, D.A., 1991. Aspects of risk assessment for hazardous pipelines containing flammable substances. J. Loss Prevent. Proc. 4(2), 68-72.

Chen, N.H., 1979. An Explicit Equation for Friction Factor in Pipe. Ind. Eng. Chem. Fun. 18(3), 296-297.

Chen, Y.S., Kim, S.W., 1987. Computation of Turbulent Flows Using an Extended k-ε Turbulence Closure Model. Document number CR-179204.

CO2PipeHaz, 2009. Quantitative Failure Consequence Hazard Assessment for Next Generation CO_2 Pipelines: The Missing Link. accessed: 12/08/13, CO2PipeHaz Project Website. http://www.co2pipehaz.eu/

Cowley, L.T., Tam, V.H.Y., 1988. Consequences of Pressurised LPG Releases: The Isle of Grain Full Scale Experiments, GASTECH 88 - 13th International LNG/LPG Conference, Kuala Lumpur.

Crowe, C.T., 2005. Multiphase Flow Handbook. CRC Press Inc., Bosa Roca, USA.

Diamantonis, N., Economou, I.G., 2011. Evaluation of Statistical Associating Fluid Theory (SAFT) and Perturbed Chain-SAFT Equations of State for the Calculation of Thermodynamic Derivative Properties of Fluids Related to Carbon Capture and Sequestration. Energ. Fuel. 25(7), 3334-3343.

Diamantonis, N.I., Boulougouris, G.C., Mansoor, E., Tsangaris, D.M., Economou, I.G., 2013. Evaluation of Cubic, SAFT, and PC-SAFT Equations of State for the Vapor-liquid Equilibrium Modeling of CO_2 Mixtures with other Gases. Ind. Eng. Chem. Res. 52(10), 3933-3942.

Diamantonis, N.I., Economou, I.G., 2012. Modeling the Phase Equilibria of a H_2O-CO_2 Mixture with PC-SAFT and tPC-PSAFT Equations of State. Mol. Phys. 110, 1205-1212.

Imperial College London, 2013. DIPPR 801 Database. accessed: 12/08/13. http://www.aiche.org/dippr/

Dixon, C.M., Gant, S.E., Obiorah, C., Bilio, M., 2012. Validation of Dispersion Models for High Pressure Carbon Dioxide Releases, IChemE Hazards XXIII. IChemE, Southport, UK, pp. 153-163.

Fairweather, M., Falle, S.A.E.G., Woolley, R.M., 2011. A Two-Dimensional, Axisymmetric Computational Fluid Dynamic Code Capable of Predicting the Near-Field Structure of High Pressure Releases of Supercritical and Multi-Phase Carbon Dioxide, Deliverable 1.4.1 CO2PipeHaz project. EU Grant Agreement 241346, http://www.co2pipehaz.eu/.

Fairweather, M., Ranson, K.R., 2003. Modelling of Underexpanded Jets Using Compressibility-Corrected, k-ε Turbulence Models, in: Hanjalic, K., Nagano, Y., Tummers, M. (Eds.), Turbulence, Heat and Mass Transfer 4. Begell House, Inc., pp. 649-656.

Fairweather, M., Ranson, K.R., 2006. Prediction of Underexpanded Jets Using Compressibility-Corrected, Two-Equation Turbulence Models. Prog. Comput. Fluid Dy. 6(1,2,3), 122-128.

Falle, S.A.E.G., 1991. Self-Similar Jets. Mon. Not. R. Astron. Soc. 250, 581-596.

GexCon AS, 2013. FLACS v10.0 User's Manual. accessed: 12/08/13. http://www.flacs.com

Gosman, A.D., Ioannides, E., 1981. Aspects of Computer Simulation of Liquid Fuelled Combustors. J. Energy 7(6), 482-490.

Harten, A., Lax, P.D., Leer, B.v., 1983. On Upstream Differencing and Godunov-Type Schemes for Hyperbolic Conservation Laws. Society for Industrial and Applied Mathematics Review 25(1), 35-61.

Ichard, M., 2012. Numerical Computations of Pressurized Liquefied Gas Releases Into the Atmosphere, Ph.D. Thesis, Department of Physics and Technology, University of Bergen, ISBN: 978-82-308-2010-0.

Jamois, D., Proust, C., Hebrard, J., Gentilhomme, O., 2013. La sécurité du captage et du stockage du CO_2: un défi pour les industries de l'énergie Récents Progrès en Génie des Procédés 104. ISBN: 978-2-910239-78-7.

Jones, W.P., Launder, B.E., 1972. The Prediction of Laminarization with a Two-Equation Model of Turbulence. Int. J. Heat Mass Tran. 15, 301-314.

Kinsman, P., Lewis, J., 2002. Report on a Second Study of Pipeline Accidents Using the Health and Safety Executive's Risk Assessment Programs MISHAP and PIPERS. HSE Books.

Launder, B.E., Spalding, D.B., 1974. The Numerical Computation of Turbulent Flows. Computer Methods in Applied Mechanics and Engineering 3, 269-289.

LeVeque, R.J., 2002. Finite Volume Methods for Hyperbolic Problems. Cambridge University Press, Cambridge.

Liu, L.-G., 1984. Compression and Phase Behavior of Solid CO_2 to Half a Megabar. Earth Planet. Sc. Lett. 71(1), 104-110.

Loth, E., 2000. Numerical Approaches for Motion of Dispersed Particles, Droplets and Bubbles. Prog. Energ. Combust. 26(3), 161-223.

Mahgerefteh, H., Brown, S., Denton, G., 2012a. Modelling the Impact of Stream Impurities on Ductile Fractures in CO_2 Pipelines. Chem. Eng. Sci. 74(1), 200-210.

Mahgerefteh, H., Brown, S., Martynov, S., 2012b. A study of the effects of friction, heat transfer, and stream impurities on the decompression behavior in CO_2 pipelines. Greenhouse Gases: Science and Technology 2, 369-379.

Mahgerefteh, H., Saha, P., Economou, I.G., 1999. Fast Numerical Simulation for Full Bore Rupture of Pressurized Pipelines. AIChE Journal 45(6), 1191-1201.

Mahgerefteh, H., Wong, S.M.A., 1999. A Numerical Blowdown Simulation Incorporating Cubic Equations of State. Comput. Chem. Eng. 23(9), 1309-1317.

Mandø, M., Lightstone, M.F., Rosendahl, L., Yin, C., Sørensen, H., 2009. Turbulence Modulation in Dilute Particle-Laden Flow. Int. J. Heat Fluid Fl. 30(2), 331-338.

Martynov, S., 2013. A Validated Heterogeneous Discharge Model, Deliverable 1.3.3 CO2PipeHaz project. EU Grant Agreement 241346, http://www.co2pipehaz.eu/.

Maxey, M.R., Riley, J.J., 1983. Equation of Motion for a Small Rigid Sphere in a Nonuniform Flow. Phys. Fluids 26(4), 883-889.

McGillivray, A., Wilday, J., 2009. Comparison of Risks from Carbon Dioxide and Natural Gas Pipelines.

Menter, F.R., 1994. Two-Equation Eddy-Viscosity Turbulence Models for Engineering Applications. AIAA Journal 32(8), 1598-1605.

Minier, J.-P., Peirano, E., 2001. The PDF Approach to Turbulent Polydispersed Two-Phase Flows. Phys. Rep. 352(9), 1-214.

Munkejord, S.T., Jakobsen, J.P., Austegard, A., Molnvik, M.J., 2010. Thermo- and fluid-dynamical modelling of two-phase multi-component carbon dioxide mixtures. Int. J. Greenh. Gas Con. 4(4), 589-596.

Narasimhamurthy, V.D., Skjold, T., Gant, S.E., 2013. On the Validation Studies of Two-Phase Models in FLACS and CFX, Deliverable 1.5.4 CO2PipeHaz project. EU Grant Agreement 241346, http://www.co2pipehaz.eu/.

National Institute for Occupational Safety and Health, 1996. Documentation for Immediately Dangerous to Life or Health Concentrations (IDLHs) for Carbon Dioxide. accessed. http://www.cdc.gov/niosh/idlh/124389.html

Peirano, E., Chibbaro, S., Pozorski, J., Minier, J.-P., 2006. Mean-Field/PDF Numerical Approach For Polydispersed Turbulent Two-phase Flows. Prog. Energ. Combust. 32(3), 315-371.

Peng, D.-Y., Robinson, D.B., 1976. A New Two-Constant Equation of State. Ind. Eng. Chem. Fun. 15(1), 59-64.

Popescu, M., 2009. Modeling of Fluid Dynamics Interacting with Ductile Fraction Propagation in High Pressure Pipeline. Acta Mech. Sinica 25(3), 311-318.

Ranz, W.E., Marshall, W.R., 1952. Evaporation from Drops. Part I. Chem. Eng. Prog. 48, 141-146.

Richards, P.J., Hoxey, R.P., 1993. Appropriate Boundary Conditions for Computational Wind Engineering Models using the k-ε Turbulence Model. J. Wind Eng. Ind. Aerod. 46/47(1), 145-153.

Richardson, S.M., Saville, G., 1996. Isle of Grain Pipeline Depressurisation Tests - OTH 94 441. HSE Books.

Sarkar, S., Erlebacher, G., Hussaini, M.Y., Kreiss, H.O., 1991. The Analysis and Modelling of Dilatational Terms in Compressible Turbulence. J. Fluid Mech. 227(1), 473-493.

Schiller, L., Naumann, A.Z., 1933. Über die grundlegenden Berechnungen bei der Schwerkraftaufbereitung. Z. Ver. Dtsch. Ing. 77(12), 318-320.

Soave, G., 1972. Equilibrium Constants from a Modified Redlich-Kwong Equation of State. Chem. Eng. Sci. 27(6), 1197-1203.

Span, R., Wagner, W., 1996. A New Equation of State for Carbon Dioxide Covering the Fluid Region from the Triple-Point Temperature to 1100 K at Pressures up to 800 MPa. J. Phys. Chem. Ref. Data 25(6), 1509-1596.

Ordnance Survey, 2013. Ordnance Survey Land and Height Products. accessed: 12/08/13. http://www.ordnancesurvey.co.uk/business-and-government/products/land-and-height-products.html

Tsangaris, D.M., Boulougouris, G., Diamantonis, N.I., Economou, I.G., 2013. Physical Properties Manual, Deliverable 1.2.6 CO2PipeHaz project. EU Grant Agreement 241346, http://www.co2pipehaz.eu/.

Versteeg, H.K., Malalasekera, W., 2007. An Introduction to Computational Fluid Dynamics The Finite Volume Method. Pearson Education Ltd.

Wareing, C.J., Woolley, R.M., Fairweather, M., Falle, S.A.E.G., 2013. A Composite Equation of State for the Modelling of Sonic Carbon Dioxide Jets. AICheE Journal. DOI: 10.1002/aic.14102.

Webber, D.M., Fannelop, T.K., Witlox, H.W.M., 1999. Source Terms for Two-Phase Flow in Long Pipelines Following an Accidental Breach, International Conference and Workshop on Modeling the Consequences of Accidental Releases of Hazardous Materials. AIChE, San Francisco, USA, pp. 145-168.

Witlox, H.W.M., Harper, M., Oke, A., 2009. Modelling of Discharge and Atmospheric Dispersion for Carbon Dioxide Releases. J. Loss Prevent. Proc. 22(6), 795-802.

Witlox, H.W.M., Harper, M., Oke, A., 2012. Phast Validation of Discharge and Atmospheric Dispersion for Carbon Dioxide Releases, Proceedings of the 15th Annual Symposium, Mary Kay O'Connor Process Safety Centre, Texas A&M University, College Station, Texas, USA.

Woolley, R.M., Fairweather, M., Wareing, C.J., Falle, S.A.E.G., Proust, C., Hebrard, J., Jamois, D., 2013. Experimental Measurement and Reynolds-Averaged Navier-Stokes Modelling of the Near-Field Structure of Multi-phase CO_2 Jet Releases. Int. J. Greenh. Gas Con. 18, 139-149.

Zeman, O., 1990. Dilational Dissipation: The Concept and Application in Modeling Compressible Mixing Layers. Phys. Fluids A-Fluid 2(2), 178-188.

11. FIGURE CAPTIONS

Figure 1. Schematic diagram of the INERIS CO_2 release test rig including sensor configuration.

Figure 2. Schematic of the experimental rig main vessel and discharge pipe, with illustratory photographs of valves and the discharge orifice.

Figure 3. Pressure vessel internal instrumentation.

Figure 4. Schematic of the orifice flange.

Figure 5. Schematic representation of the use of a subgrid to model the flow through a small diameter puncture at the end of a pipe.

Figure 6. Elevation variation along pipeline route.

Figure 7. Upstream section, predicted release pressure, plotted against time for cases with and without inclination.

Figure 8. Downstream section, predicted release pressure, plotted against time for cases with and without inclination.

Figure 9. Total predicted mass discharge rate plotted against time for cases with and without inclination.

Figure 10. Graphical representation of SAFT equation of state components.

Figure 11. Predictions and data of the isothermal compressibility of a quaternary CO_2-containing system plotted against pressure. Experimental data from Alsiyabi et al. (2012).

Figure 12. Adaptive mesh refinement grid mapped onto mean velocity predictions in the region of a Mach disc.

Figure 13. CO_2 internal energy predictions on the saturation line obtained using the composite equation of state, showing gaseous and dense phases.

Figure 14. Axial temperature and O_2 mole fraction predictions plotted against experimental data (symbols) for Tests 2.

Figure 15. Radial temperature profiles of Test 8 at axial distances of 1, 2 and 5 m (lines – predictions, symbols – data).

Figure 16. Schematic of modelled crater shape and dimensions.

Figure 17. Sample three-dimensional geometry of a typical full-bore guillotine rupture into an elliptic crater. (a) View at x=0 depicting the crater length, and (b) view at z=0 depicting the crater plan.

Figure 18. Sample three-dimensional model predictions of a typical full-bore guillotine rupture into a crater. (a) Dense-phase CO_2 mass fraction, and (b) total velocity.

Figure 19. Near-field model predictions observed on a cross-sectional plane above the crater just above ground level.

Figure 20. Near-field model predictions observed on a cross-sectional plane above the crater just above ground level.

Figure 21. Terrain data depicting grid methodologies, and coloured according to height topography, loaded in FLACS (left) and CFX (right).

Figure 22. Predicted CO_2 jet in the vicinity of the crater using FLACS (left) and CFX (right).

Figure 23. CFX predicted steady-state CO_2 cloud, defined using three different mean CO_2 concentrations: 1% v/v (left); 2% v/v (middle); 4% v/v (right), and coloured according to the distance from the crater source.

Figure 24. Snapshots of the CO_2 cloud at different time intervals, predicted by the FLACS model at (a) t = 10 s; (b) t = 150 s; (c) t = 240 s; and (d) t = 540 s. Here FMOLE (v/v) corresponds to volume fraction of CO_2.

Figure 25. Schematic representation of the thermo-physical modelling strategy.

12. TABLE CAPTIONS

Table 1. Parameters of the experimental releases.

Table 2. Discharge properties predicted using various equations of state in comparison with the measured values for Test 2 (Table 1).

Table 3. Discharge properties predicted using various equations of state in comparison with the measured values for Test 8 (Table 1).

Table 4. Derivative properties useful in the current work.

Table 5. Far-field source terms integrated from near-field calculations

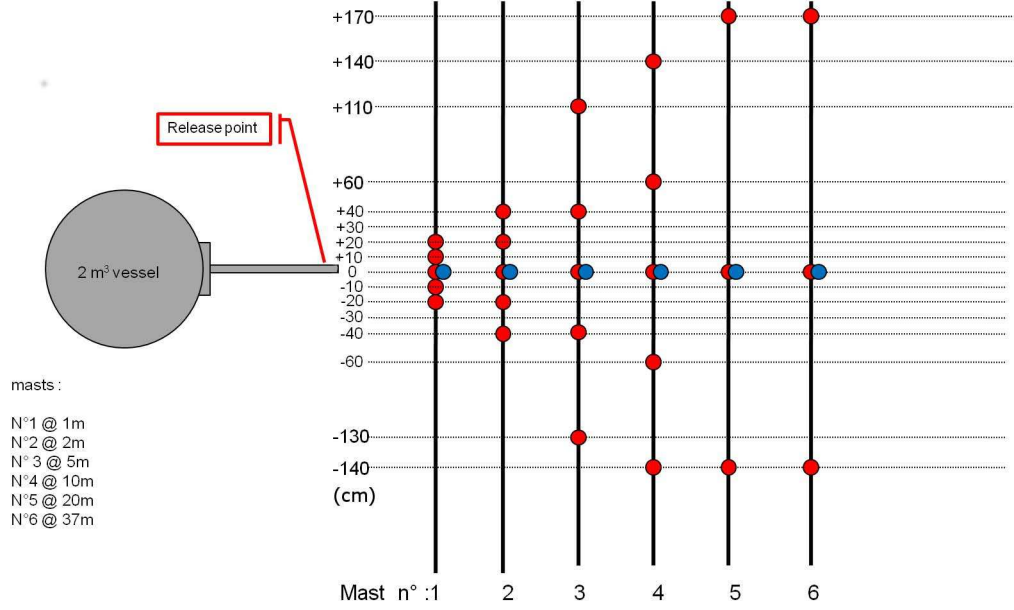
Release point
2 m3 vessel
masts :
N°1 @ 1m
N°2 @ 2m
N° 3 @ 5m
N°4 @ 10m
N°5 @ 20m
N°6 @ 37m
+170
+140
+110
+60
+40
+30
+20
+10
0
-10
-20
-30
-40
-60
-130
-140
(cm)
Mast n° :1
2
3
4
5
6

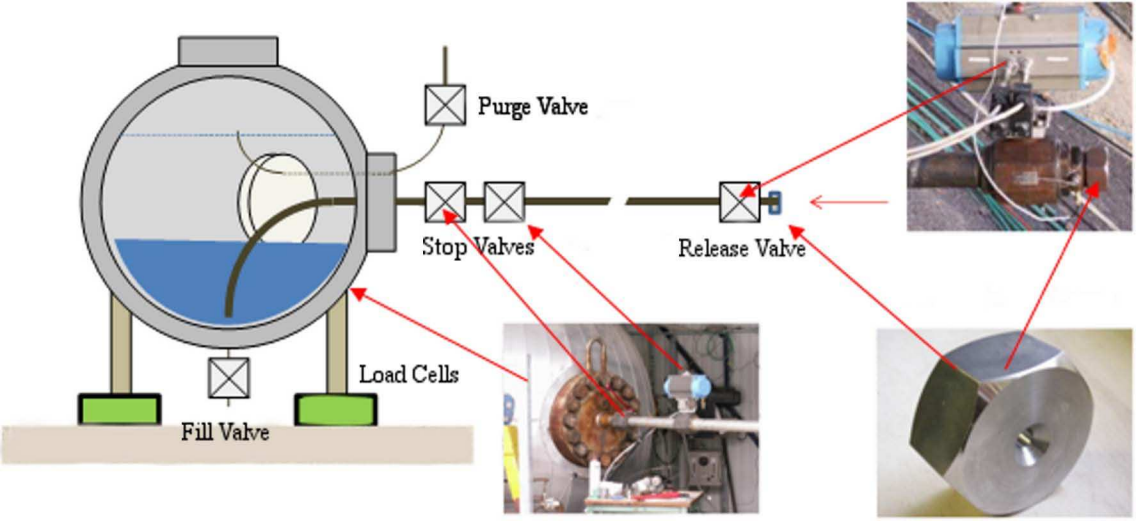
Purge Valve
Stop Valves
Release Valve
Load Cells
Fill Valve

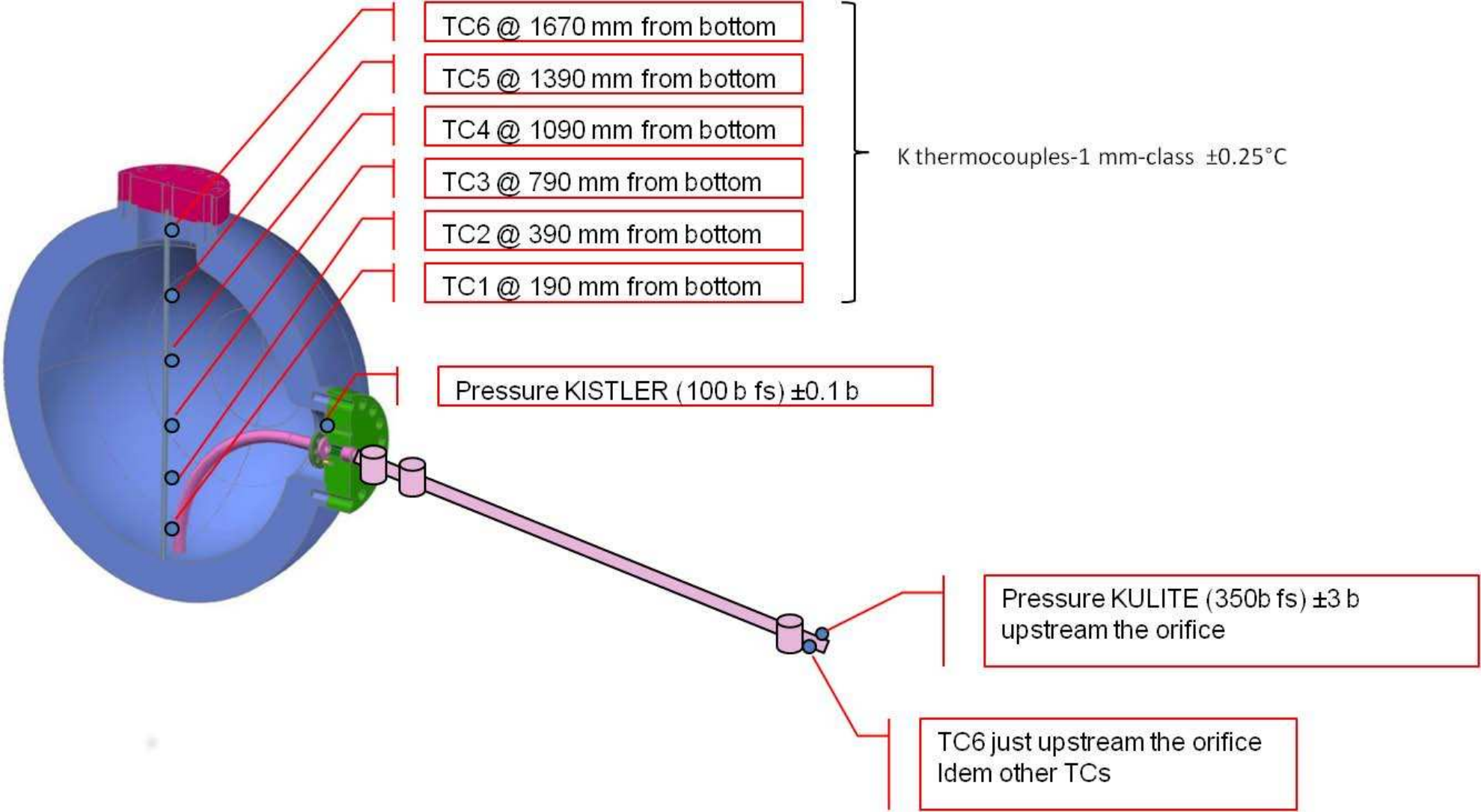
TC6 @ 1670 mm from bottom
TC5 @ 1390 mm from bottom
TC4 @ 1090 mm from bottom
TC3 @ 790 mm from bottom
TC2 @ 390 mm from bottom
TC1 @ 190 mm from bottom
K thermocouples-1 mm-class ±0.25°C
Pressure KISTLER (100 b fs) ±0.1 b
Pressure KULITE (350b fs) ±3 b
upstream the orifice
TC6 just upstream the orifice
Idem other TCs

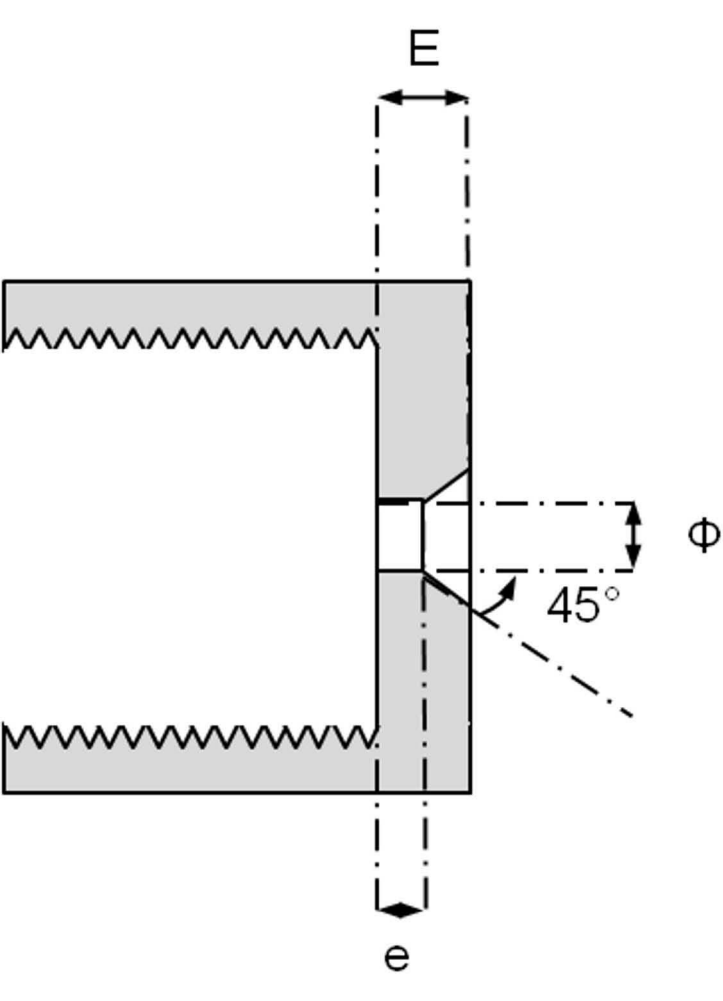
E
Φ
45°
e

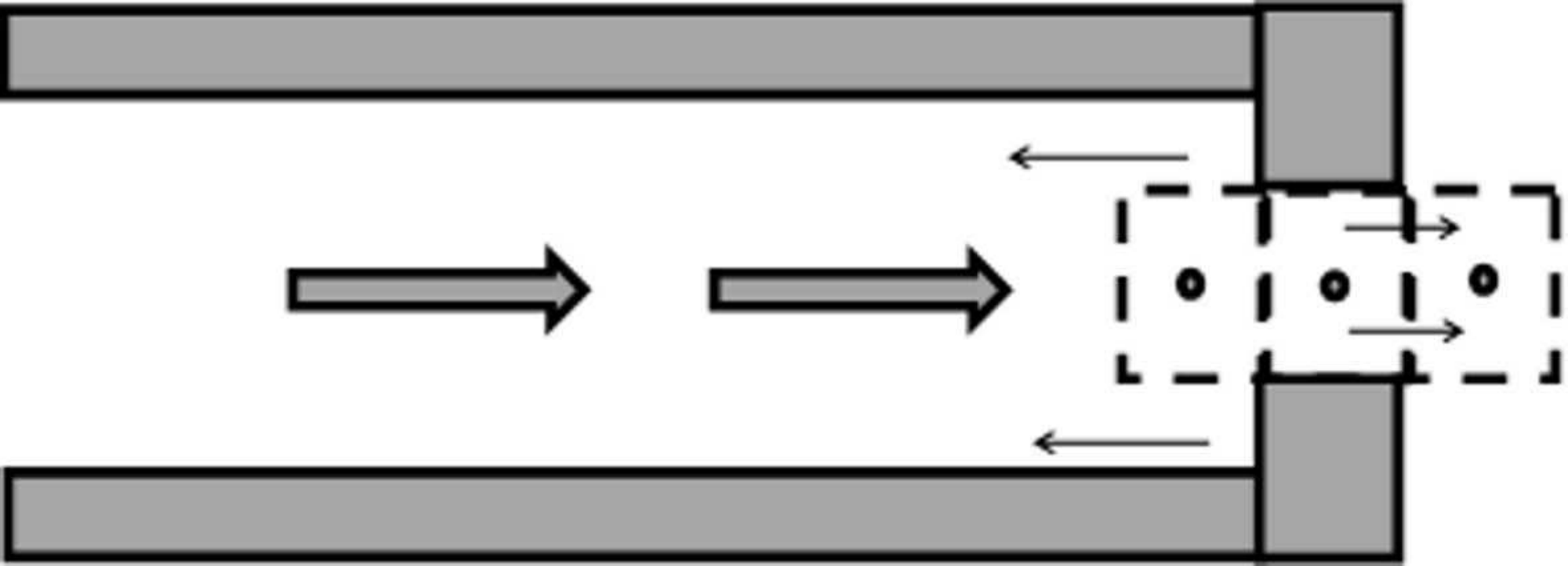

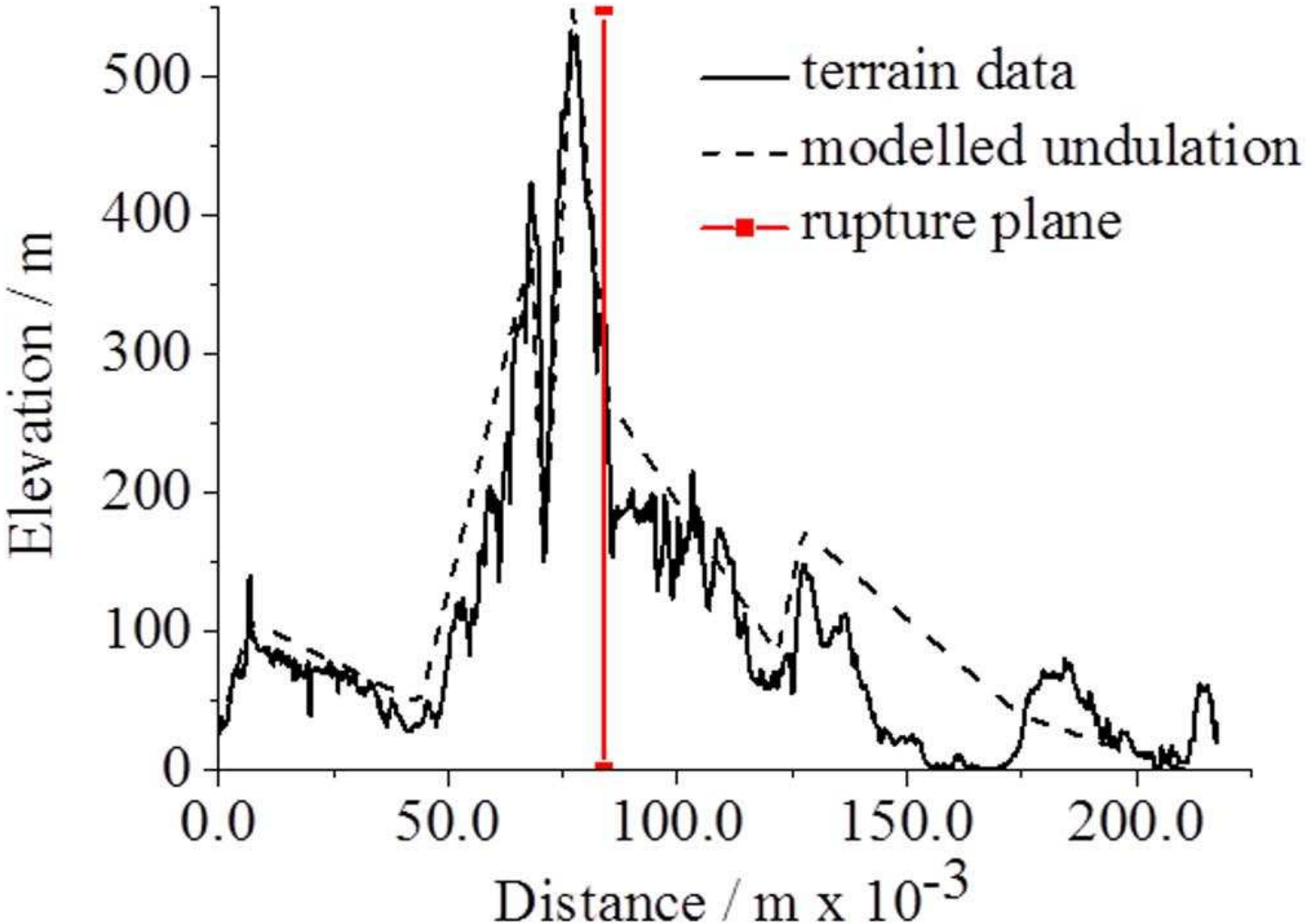
terrain data
modelled undulation
rupture plane
Elevation / m
500
400
300
200
100
0
0.0
50.0
100.0
150.0
200.0
Distance / m x 10-3

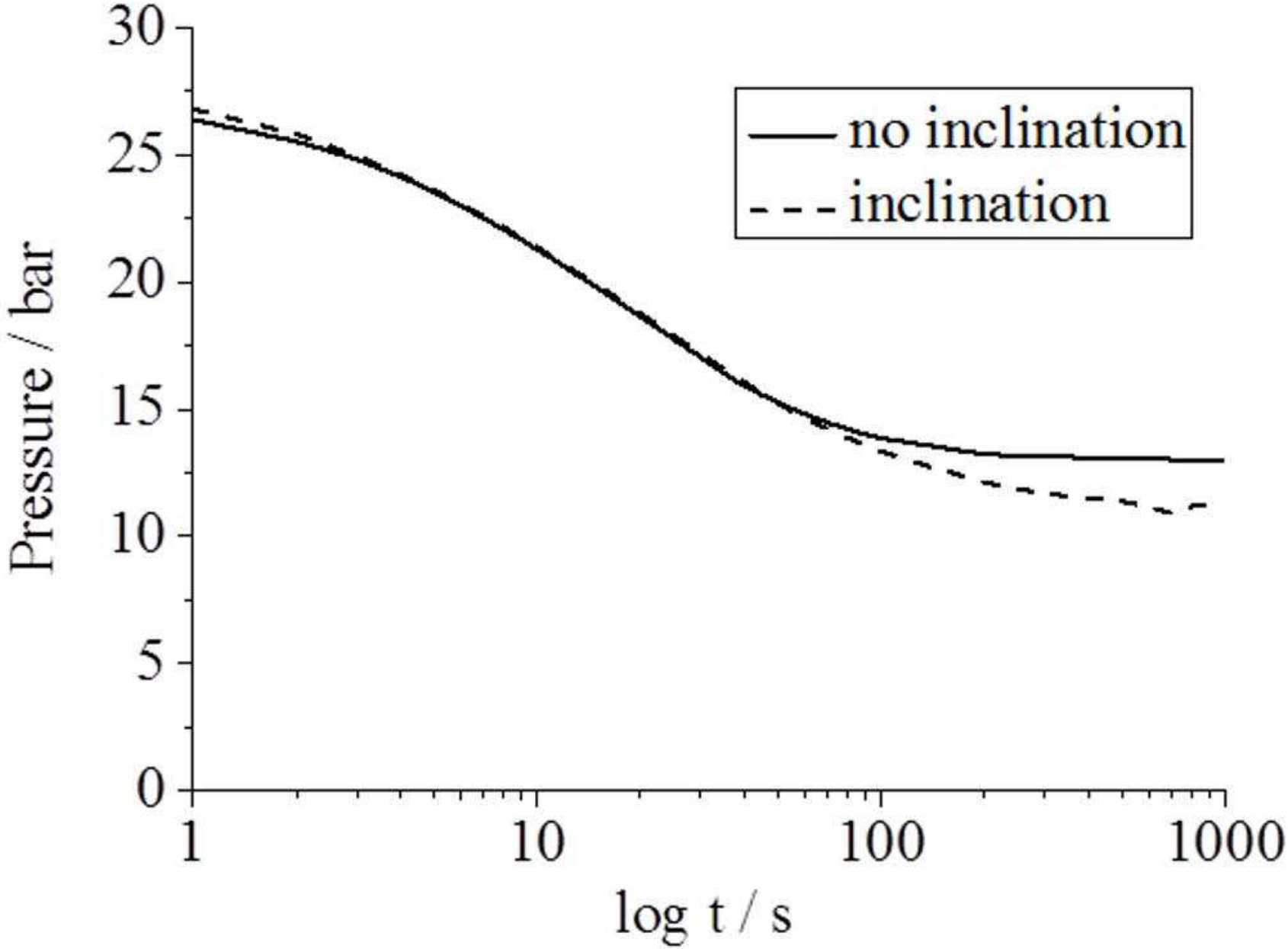
30
25
20
15
10
5
0
Pressure / bar
1
10
100
1000
log t / s
no inclination
inclination

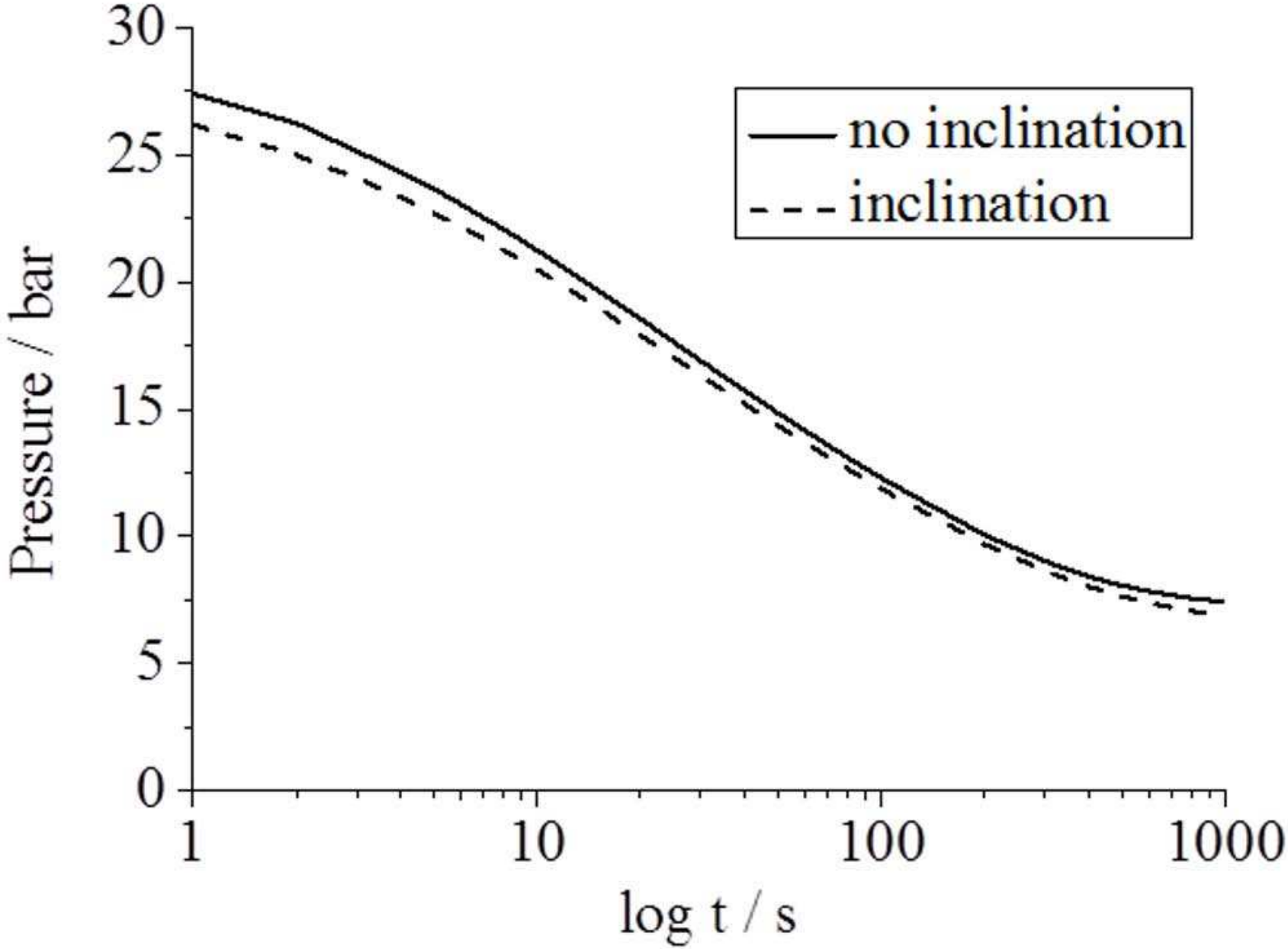
30
25
20
15
10
5
0
Pressure / bar
1
10
100
1000
log t / s
no inclination
inclination

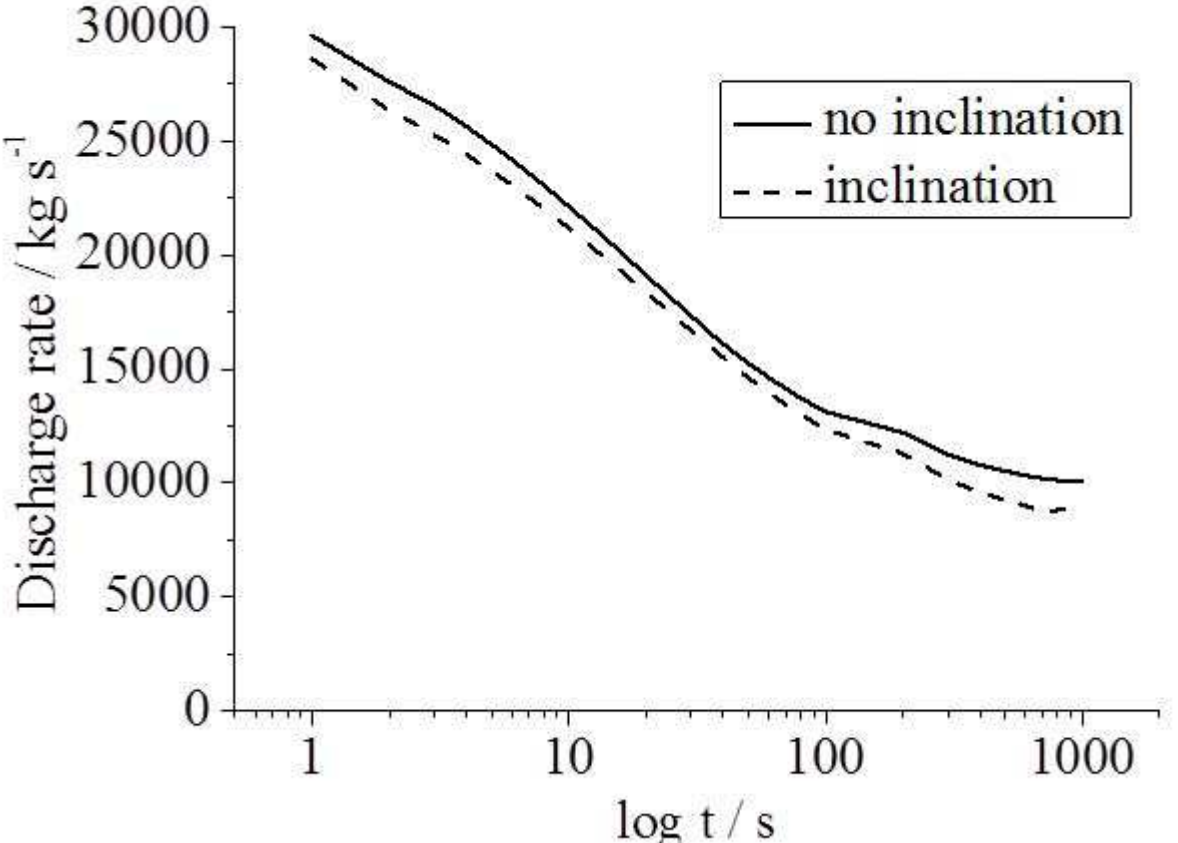
30000
25000
20000
15000
10000
5000
0
Discharge rate / kg s-1
1
10
100
1000
log t / s
no inclination
inclination

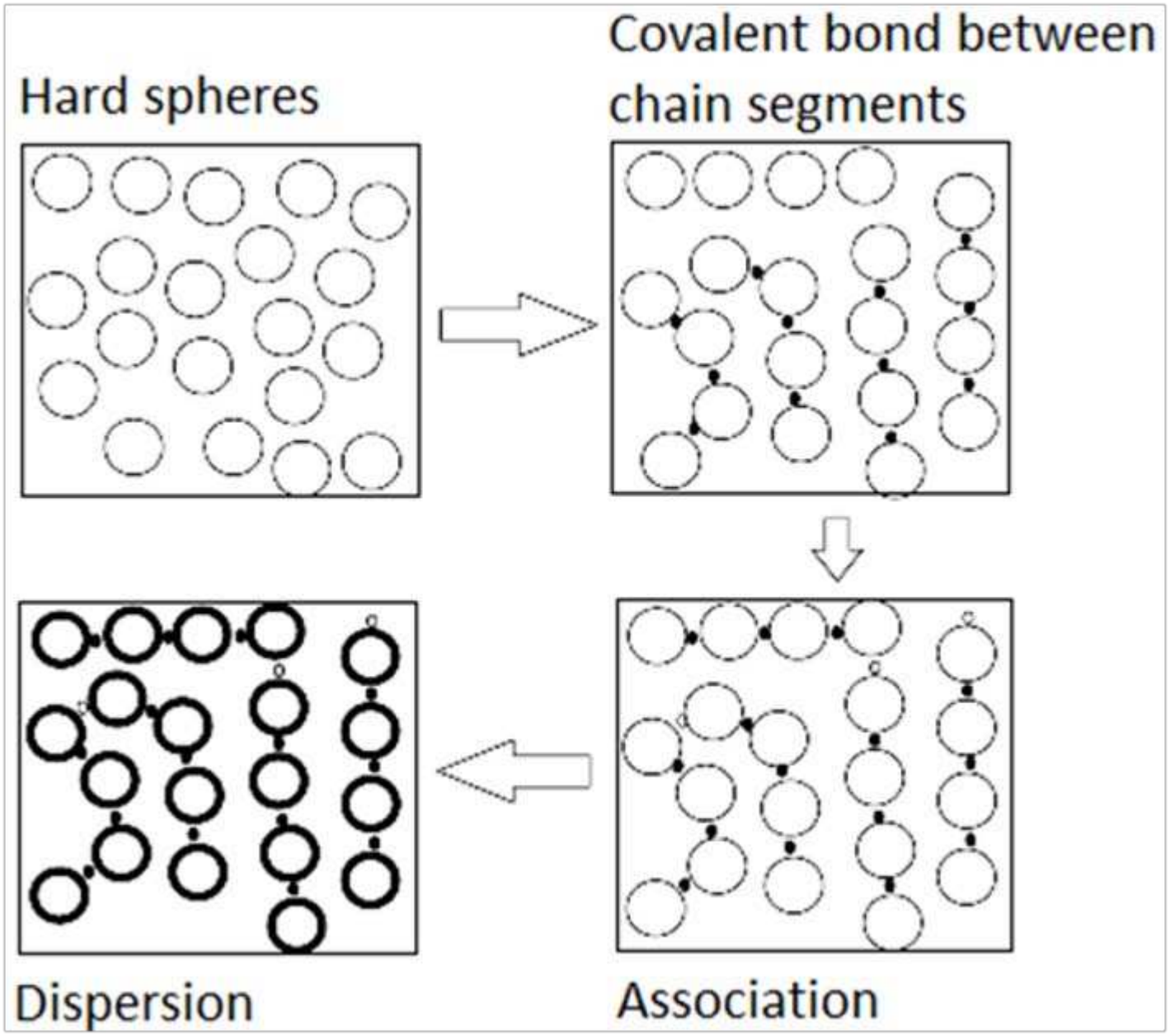
Hard spheres
Covalent bond between chain segments
Dispersion
Association

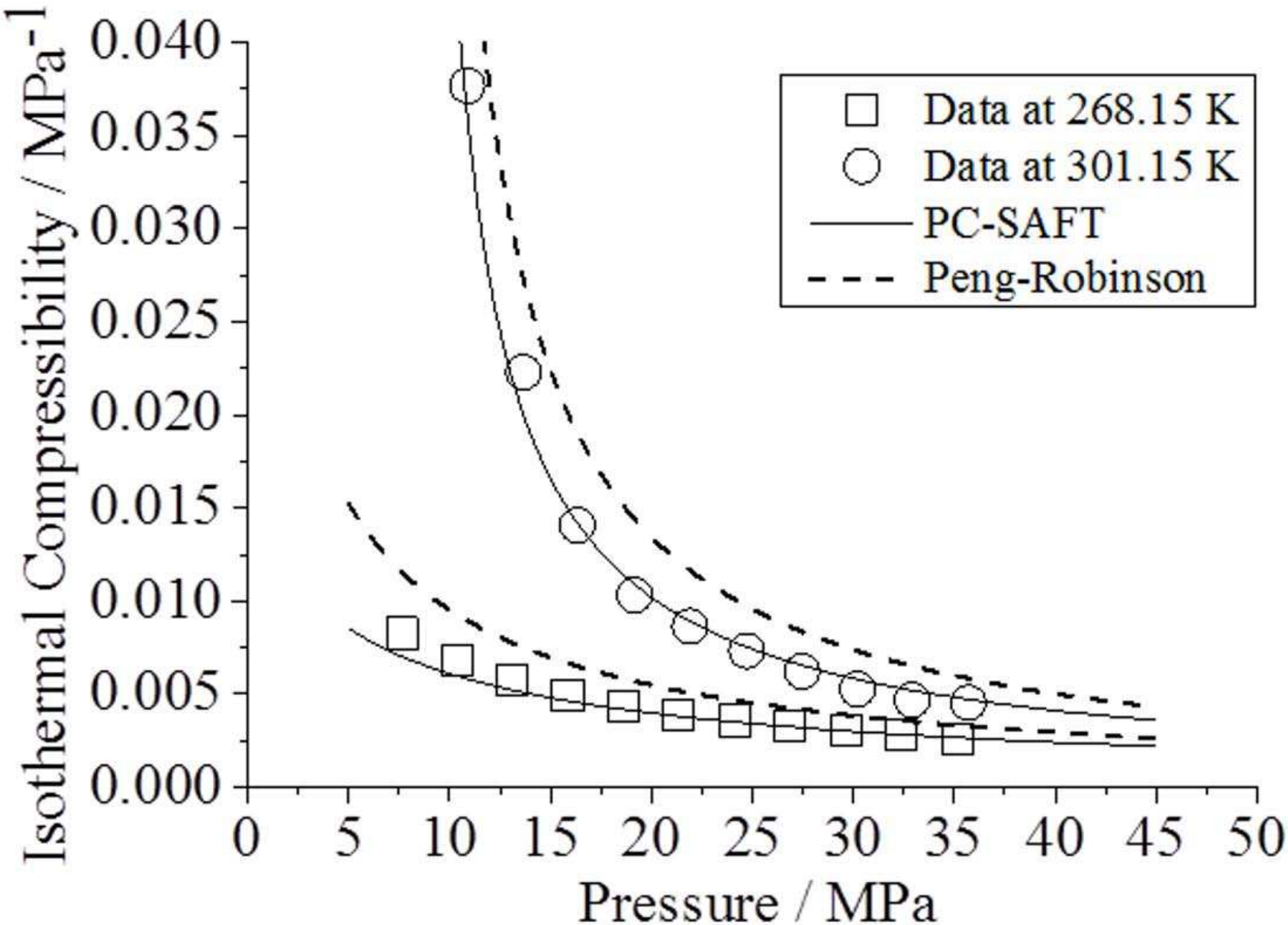
Isothermal Compressibility / MPa-1
0.040
0.035
0.030
0.025
0.020
0.015
0.010
0.005
0.000
0
5
10
15
20
25
30
35
40
45
50
Pressure / MPa
Data at 268.15 K
Data at 301.15 K
PC-SAFT
Peng-Robinson

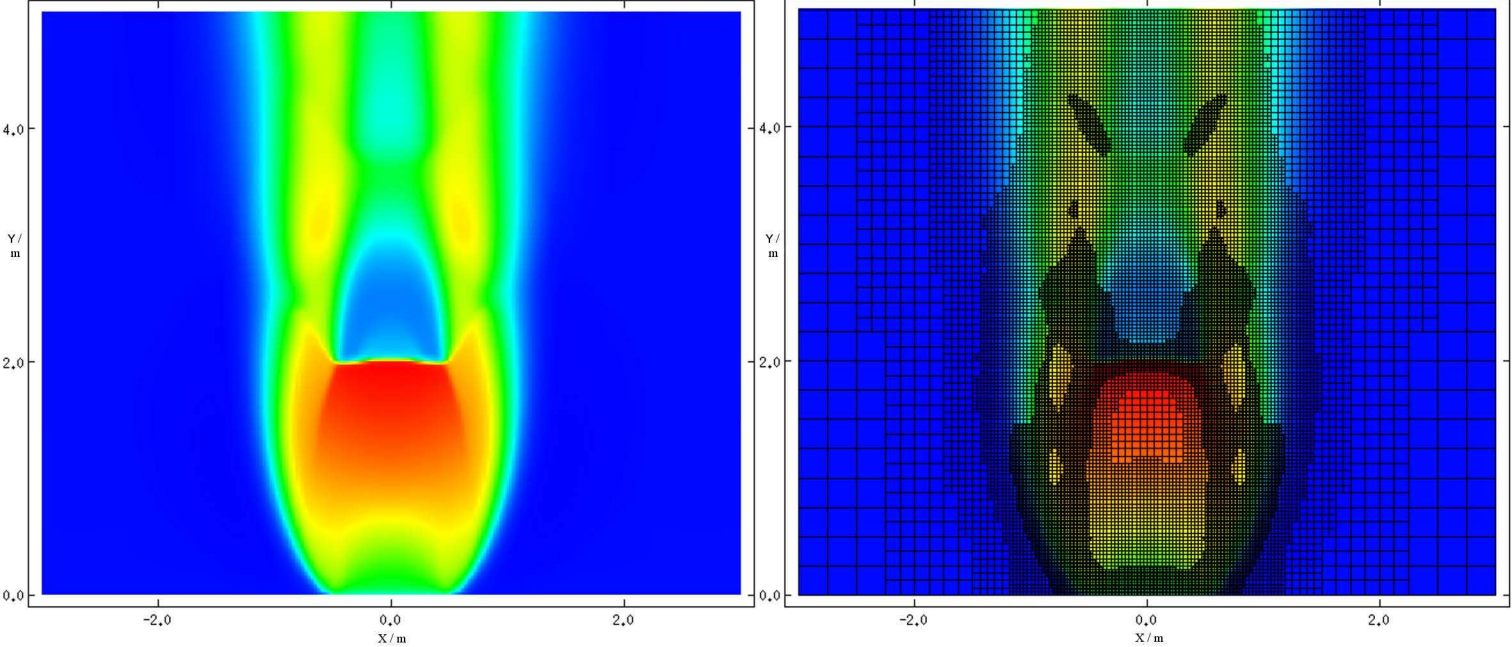
4.0
Y/
m
2.0
0.0
-2.0
0.0
2.0
X/m
4.0
Y/
m
2.0
0.0
-2.0
0.0
2.0
X/m

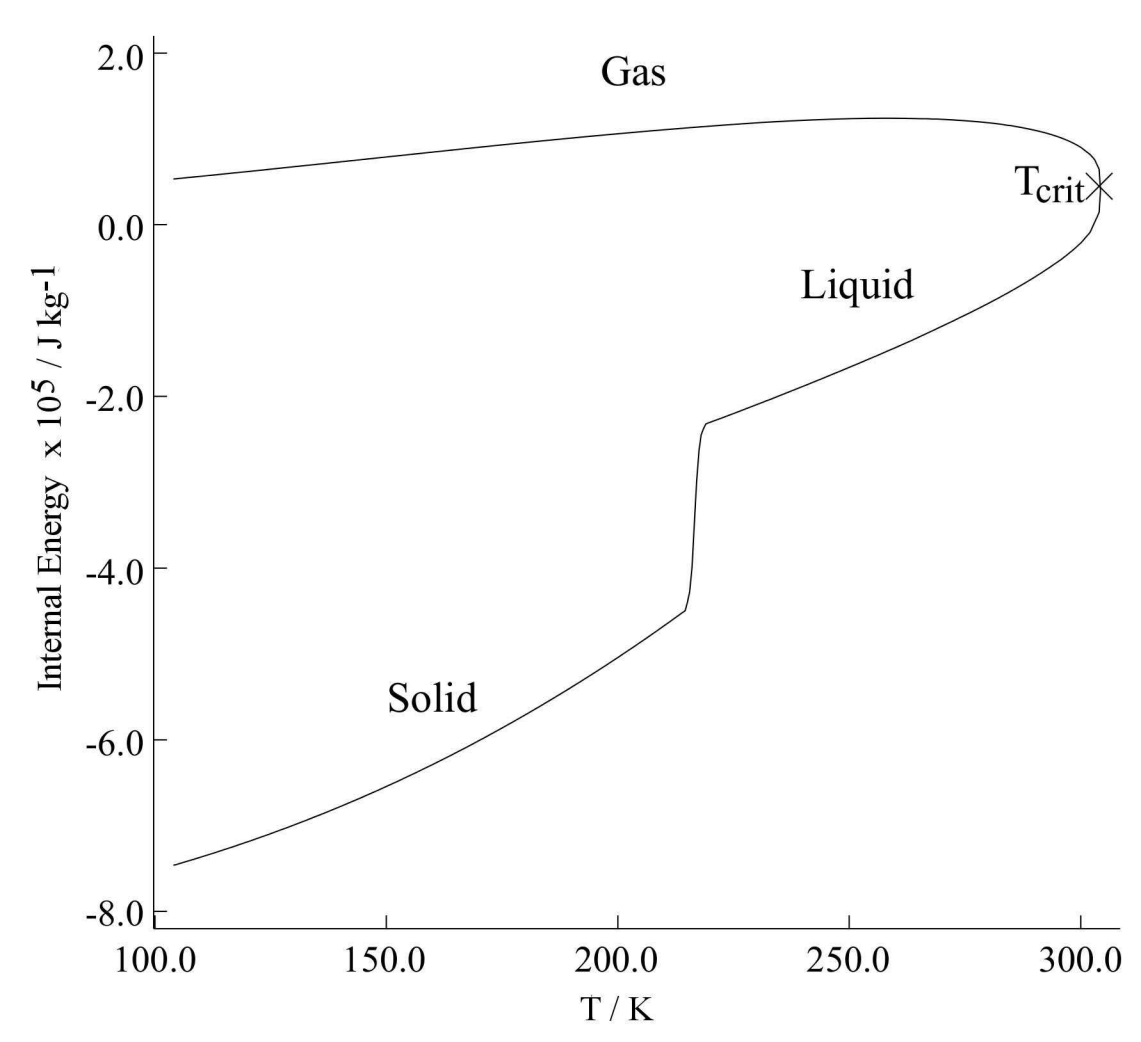
Gas
Liquid
Solid
T_{crit}
2.0
0.0
-2.0
-4.0
-6.0
-8.0
Internal Energy x 10^5 / J kg-1
100.0
150.0
200.0
250.0
300.0
T / K

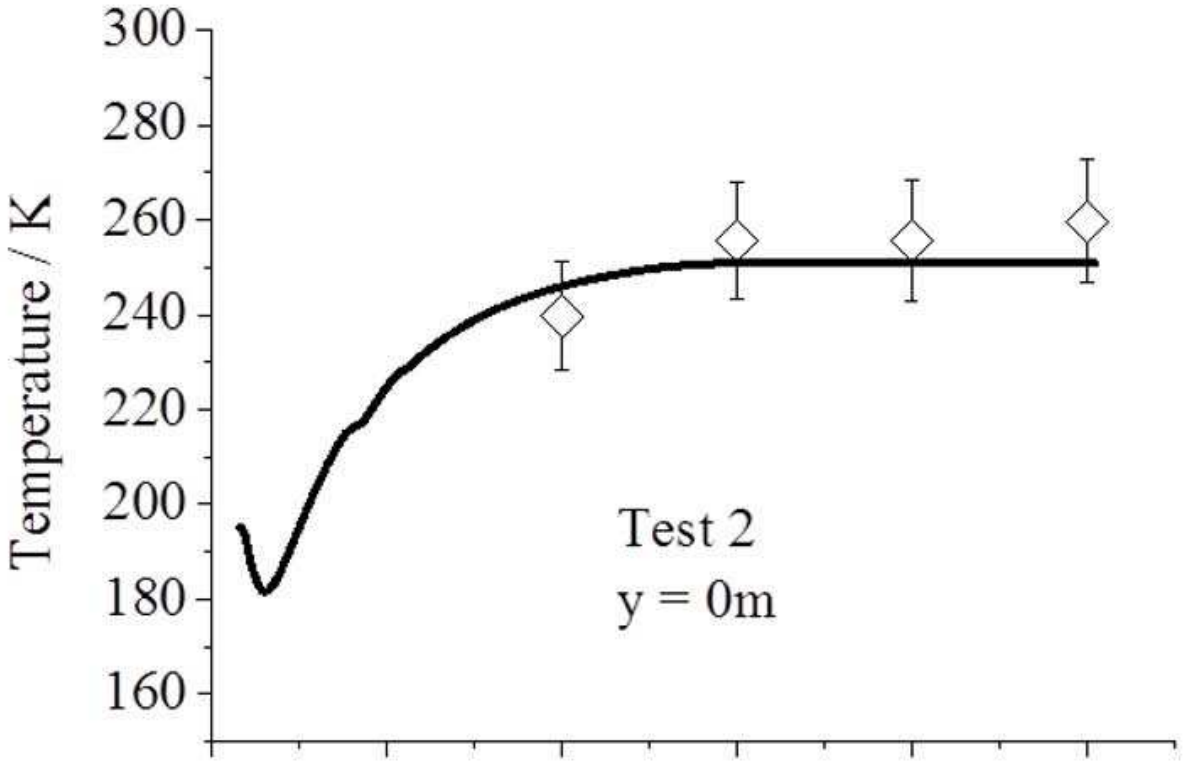
Temperature / K
300
280
260
240
220
200
180
160
Test 2
y = 0m

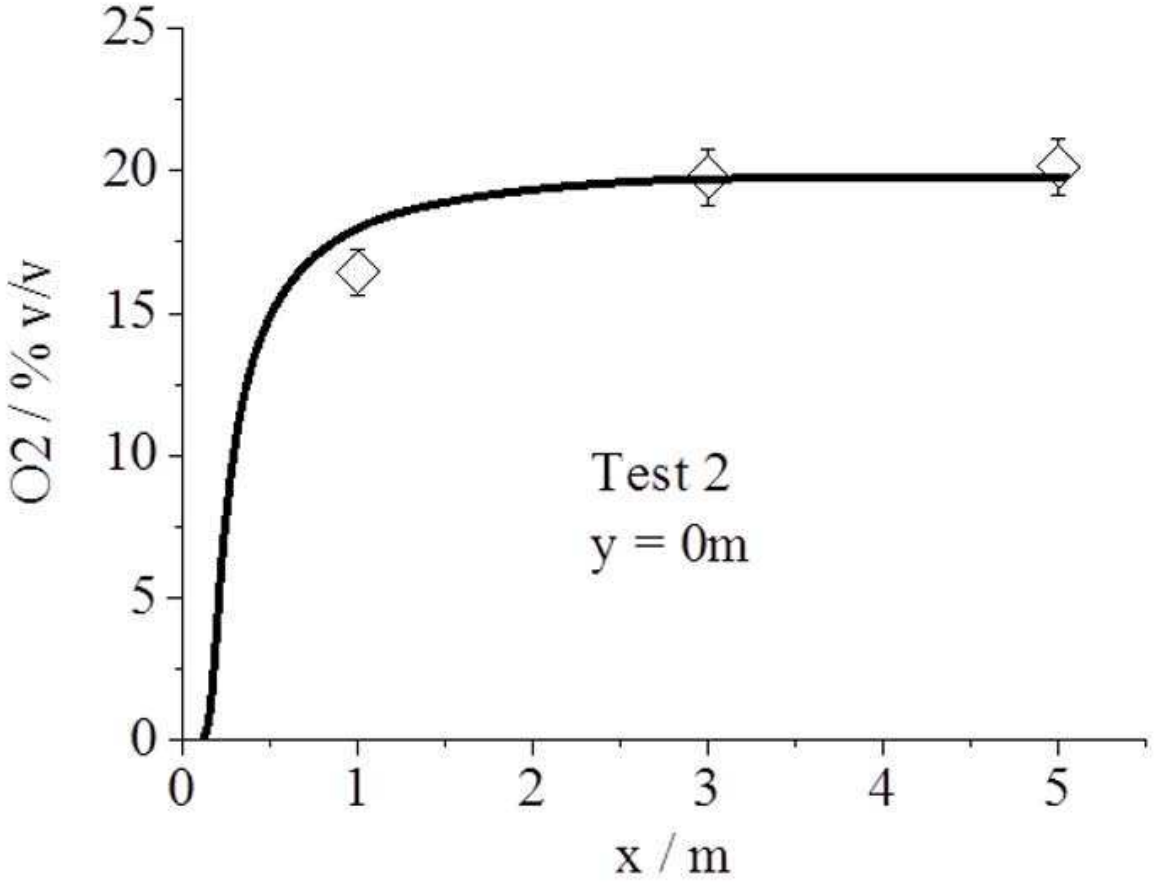
O2 / % v/v
25
20
15
10
5
0
0
1
2
3
4
5
x / m
Test 2
y = 0m

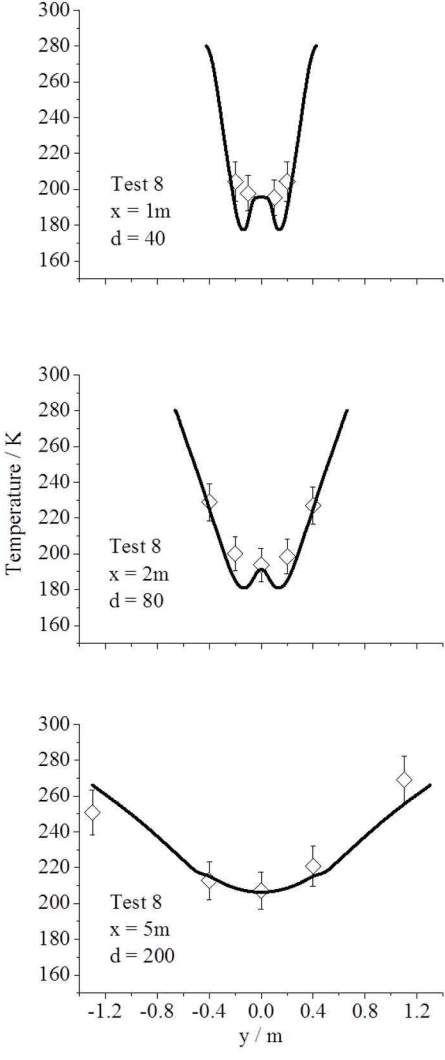
Temperature / K
300
280
260
240
220
200
180
160
Test 8
x = 1m
d = 40
Test 8
x = 2m
d = 80
Test 8
x = 5m
d = 200
-1.2
-0.8
-0.4
0.0
0.4
0.8
1.2
y / m

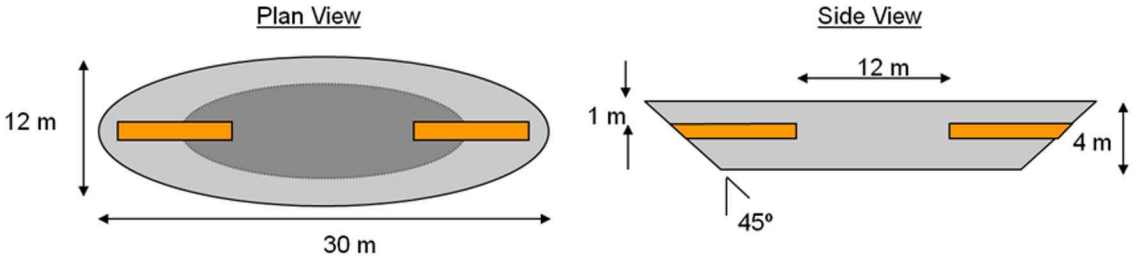
Plan View
12 m
30 m
Side View
12 m
1 m
4 m
45º

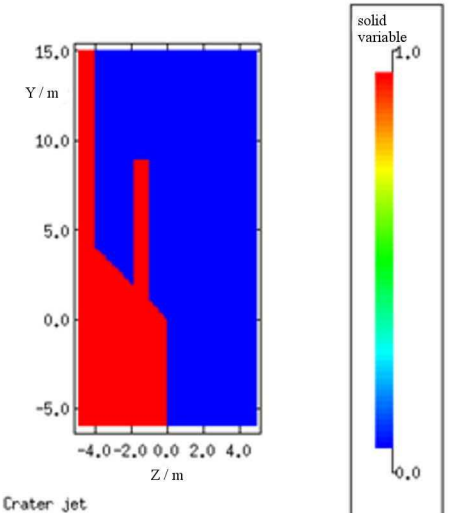
15.0
Y / m
10.0
5.0
0.0
-5.0
-4.0 -2.0 0.0 2.0 4.0
Z / m
Crater jet
solid
variable
1.0
0.0

(a)

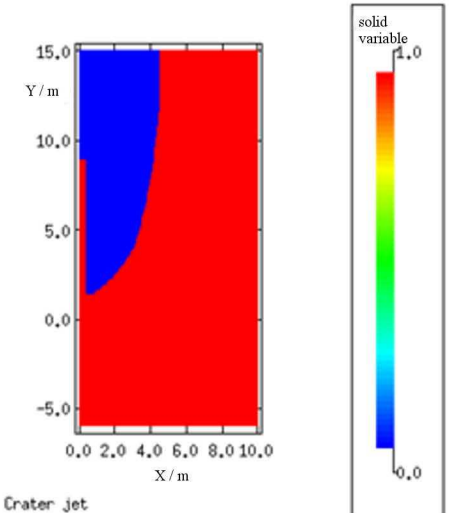
15.0
Y / m
10.0
5.0
0.0
-5.0
0.0 2.0 4.0 6.0 8.0 10.0
X / m
Crater jet
solid
variable
1.0
0.0

(b)

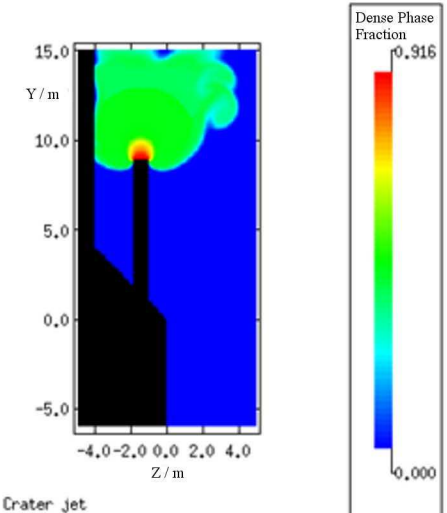
Dense Phase Fraction
0.916
0.000
15.0
10.0
5.0
0.0
-5.0
Y / m
-4.0 -2.0 0.0 2.0 4.0
Z / m
Crater jet

(a)

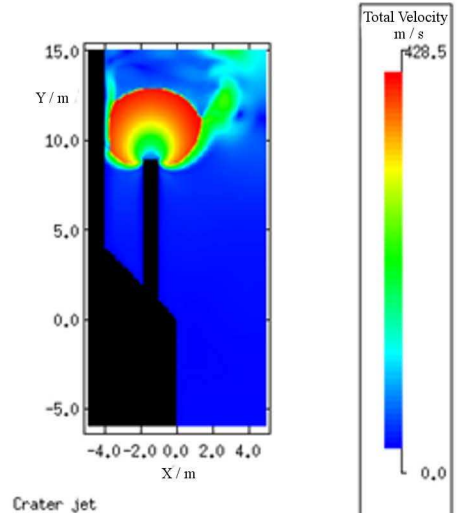
Total Velocity
m / s
428.5
0.0
15.0
10.0
5.0
0.0
-5.0
Y / m
-4.0 -2.0 0.0 2.0 4.0
X / m
Crater jet

(b)

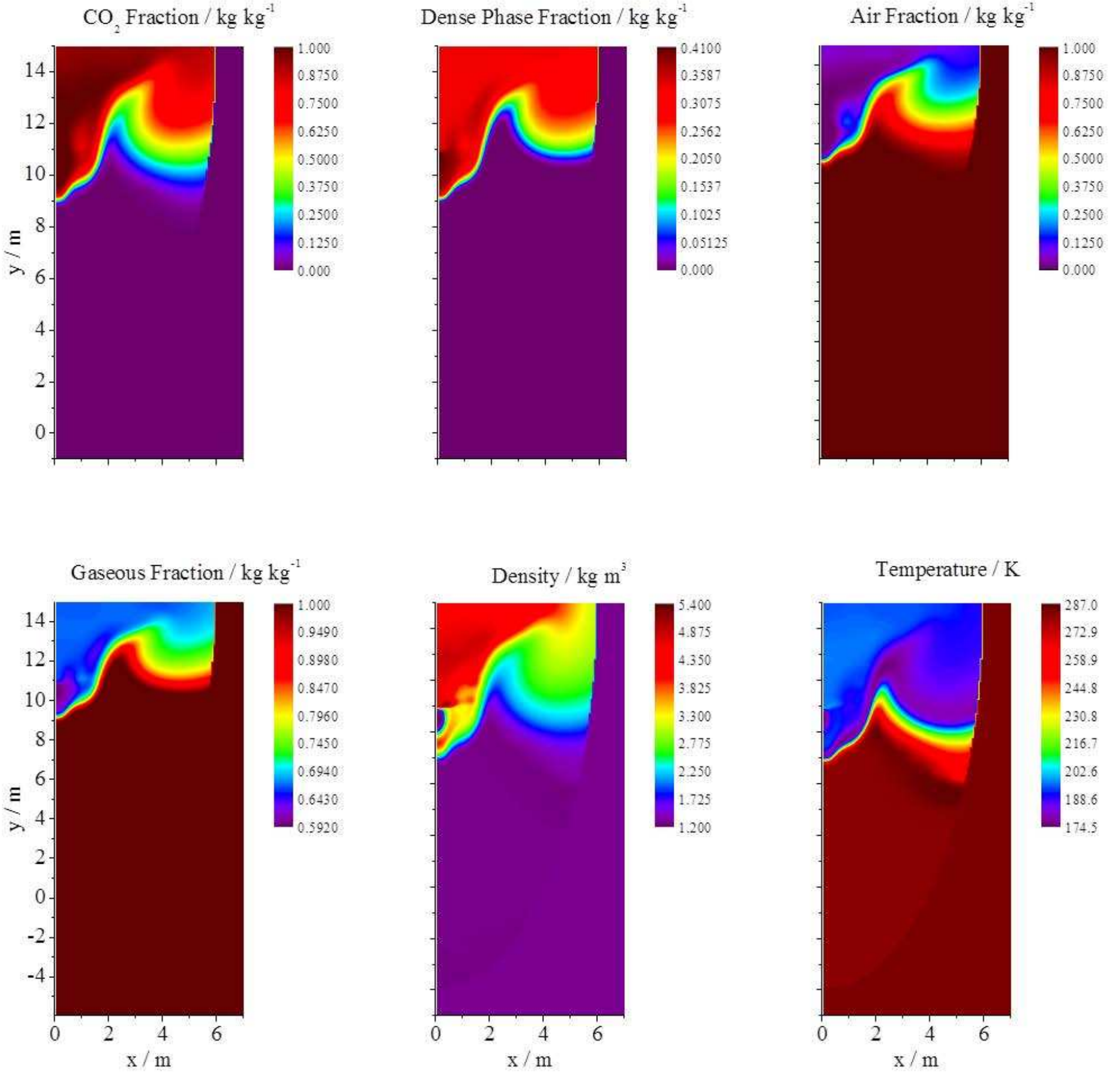
CO2 Fraction / kg kg-1
1.000
0.8750
0.7500
0.6250
0.5000
0.3750
0.2500
0.1250
0.000
Dense Phase Fraction / kg kg-1
0.4100
0.3587
0.3075
0.2562
0.2050
0.1537
0.1025
0.05125
0.000
Air Fraction / kg kg-1
1.000
0.8750
0.7500
0.6250
0.5000
0.3750
0.2500
0.1250
0.000
Gaseous Fraction / kg kg-1
1.000
0.9490
0.8980
0.8470
0.7960
0.7450
0.6940
0.6430
0.5920
Density / kg m3
5.400
4.875
4.350
3.825
3.300
2.775
2.250
1.725
1.200
Temperature / K
287.0
272.9
258.9
244.8
230.8
216.7
202.6
188.6
174.5
y / m
x / m

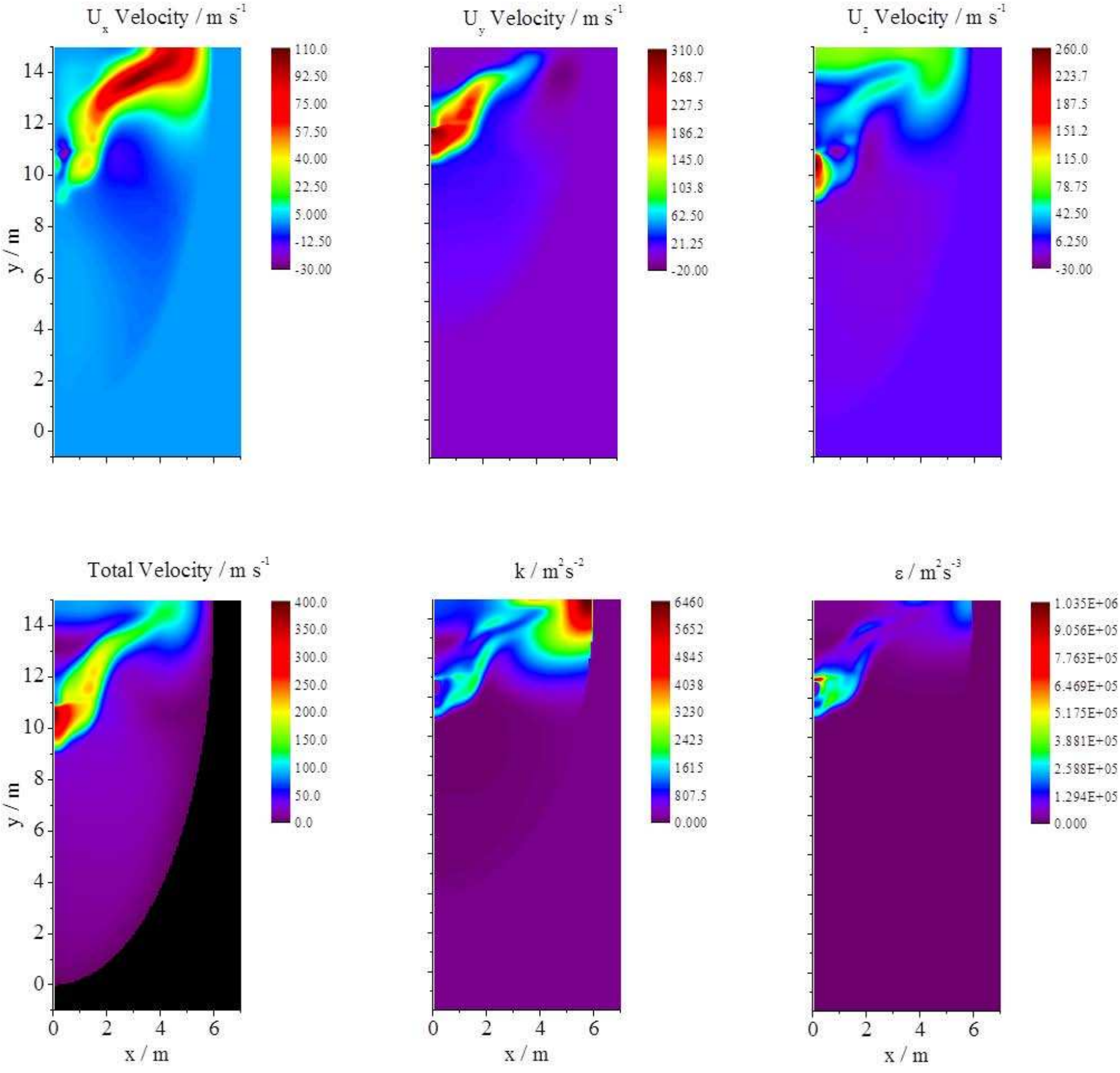
U_x Velocity / m s^-1
110.0
92.50
75.00
57.50
40.00
22.50
5.000
-12.50
-30.00
U_y Velocity / m s^-1
310.0
268.7
227.5
186.2
145.0
103.8
62.50
21.25
-20.00
U_z Velocity / m s^-1
260.0
223.7
187.5
151.2
115.0
78.75
42.50
6.250
-30.00
Total Velocity / m s^-1
400.0
350.0
300.0
250.0
200.0
150.0
100.0
50.0
0.0
k / m^2 s^-2
6460
5652
4845
4038
3230
2423
1615
807.5
0.000
ε / m^2 s^-3
1.035E+06
9.056E+05
7.763E+05
6.469E+05
5.175E+05
3.881E+05
2.588E+05
1.294E+05
0.000
y / m
x / m
0
2
4
6
8
10
12
14

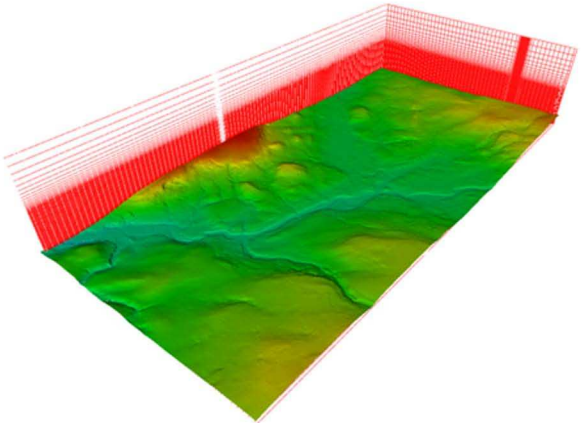

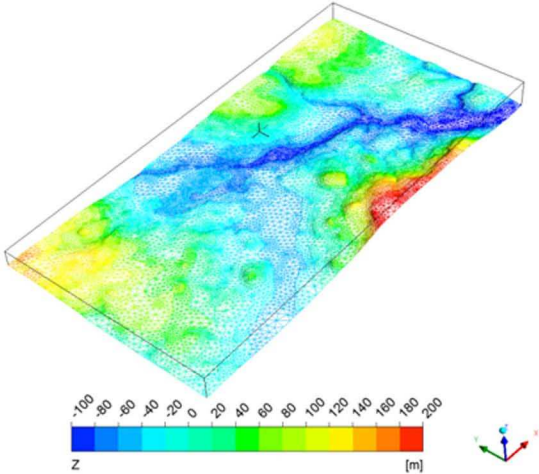
-100
-80
-60
-40
-20
0
20
40
60
80
100
120
140
160
180
200
Z
[m]

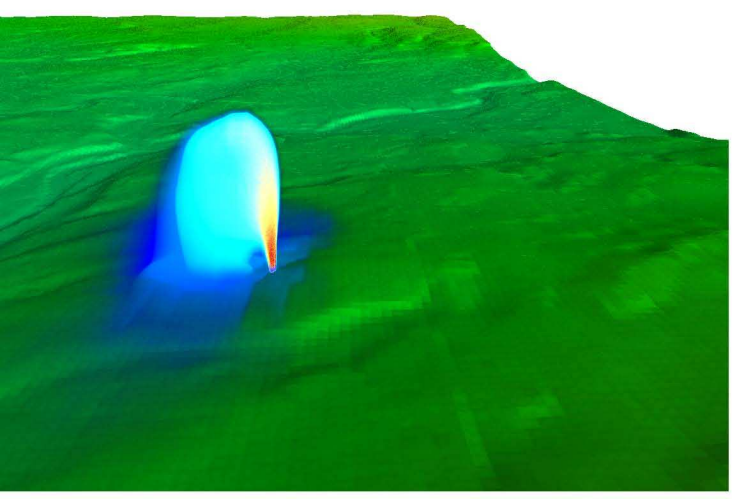

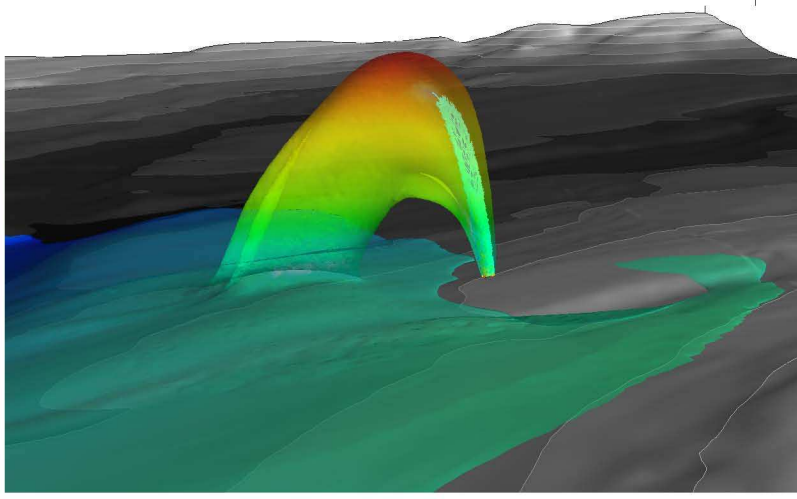

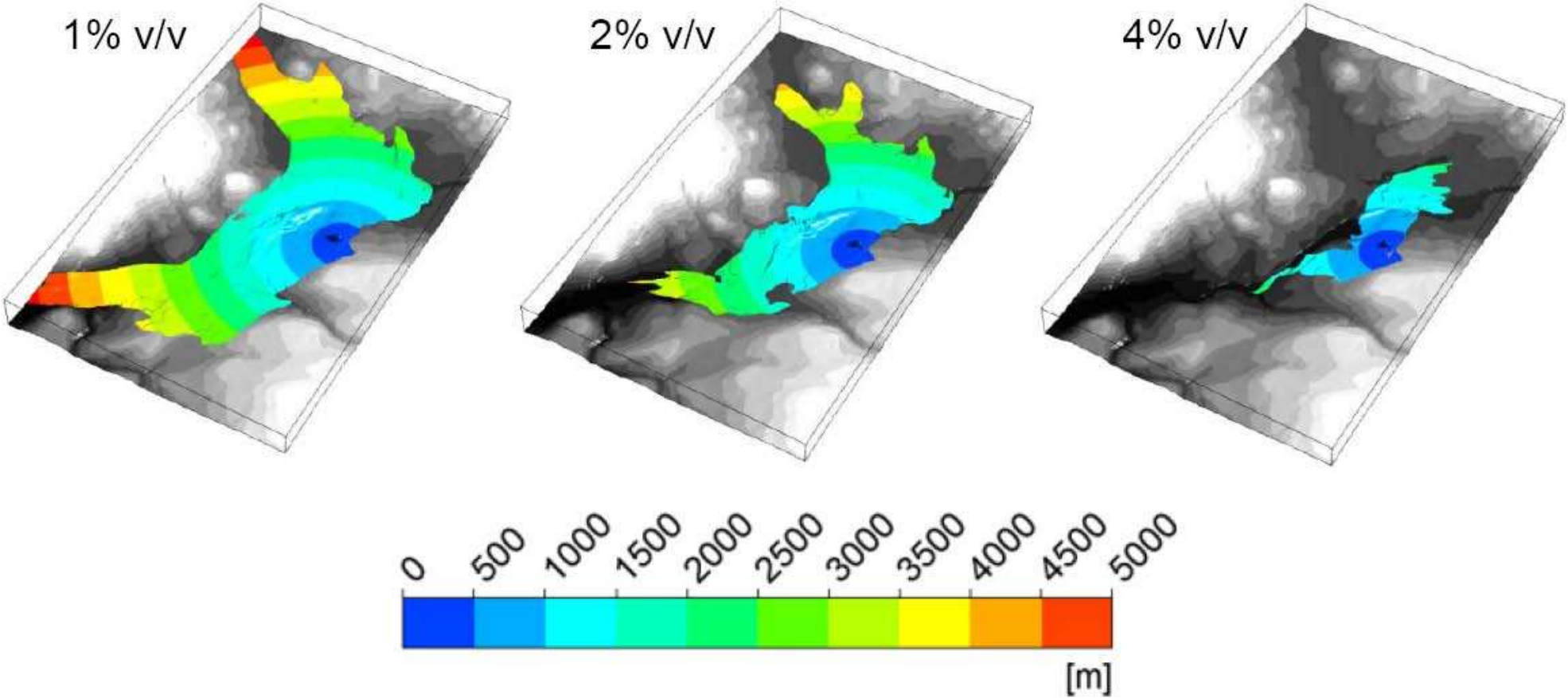
1% v/v
2% v/v
4% v/v
0
500
1000
1500
2000
2500
3000
3500
4000
4500
5000
[m]

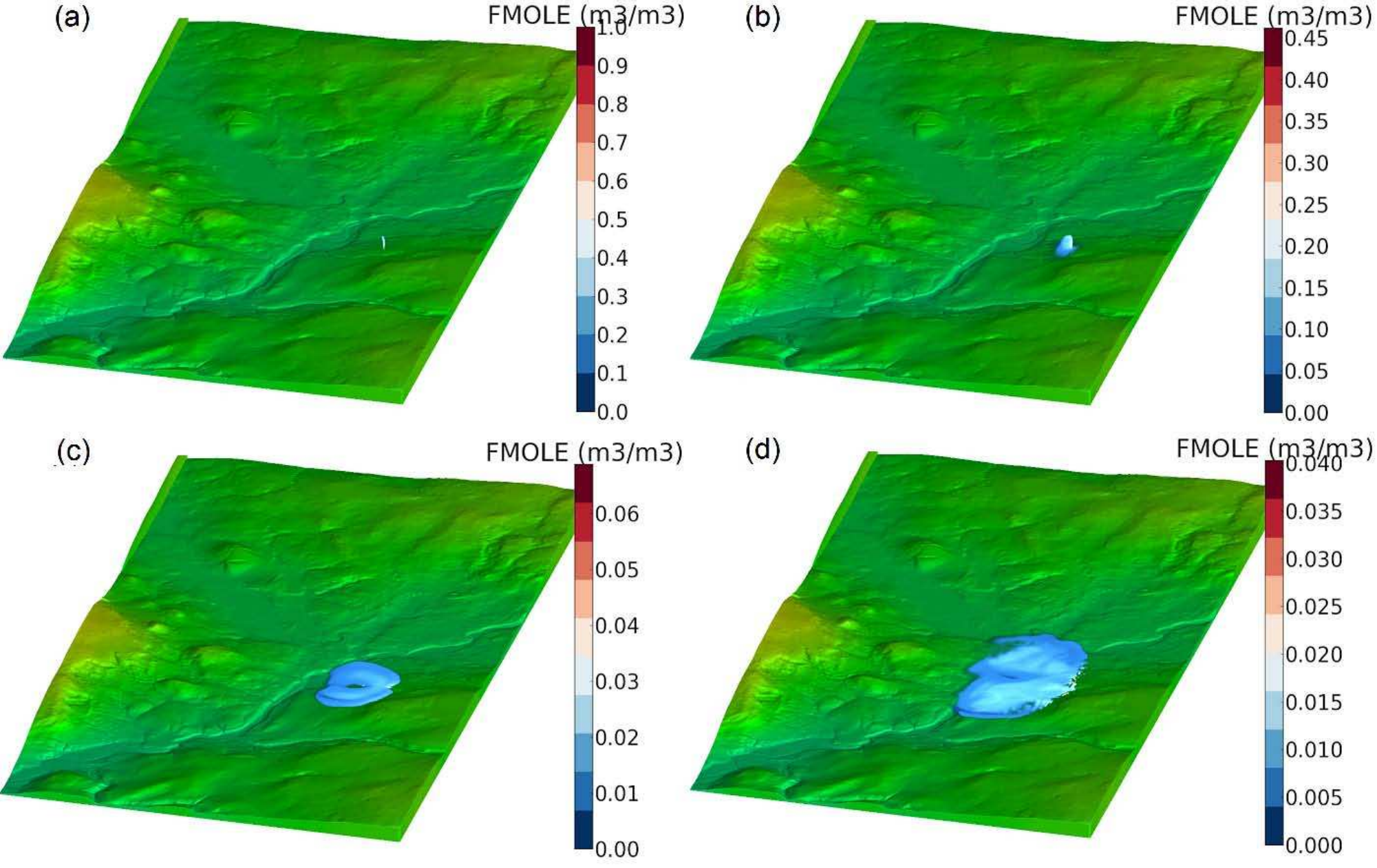
(a)
FMOLE (m3/m3)
1.0
0.9
0.8
0.7
0.6
0.5
0.4
0.3
0.2
0.1
0.0
(b)
FMOLE (m3/m3)
0.45
0.40
0.35
0.30
0.25
0.20
0.15
0.10
0.05
0.00
(c)
FMOLE (m3/m3)
0.06
0.05
0.04
0.03
0.02
0.01
0.00
(d)
FMOLE (m3/m3)
0.040
0.035
0.030
0.025
0.020
0.015
0.010
0.005
0.000

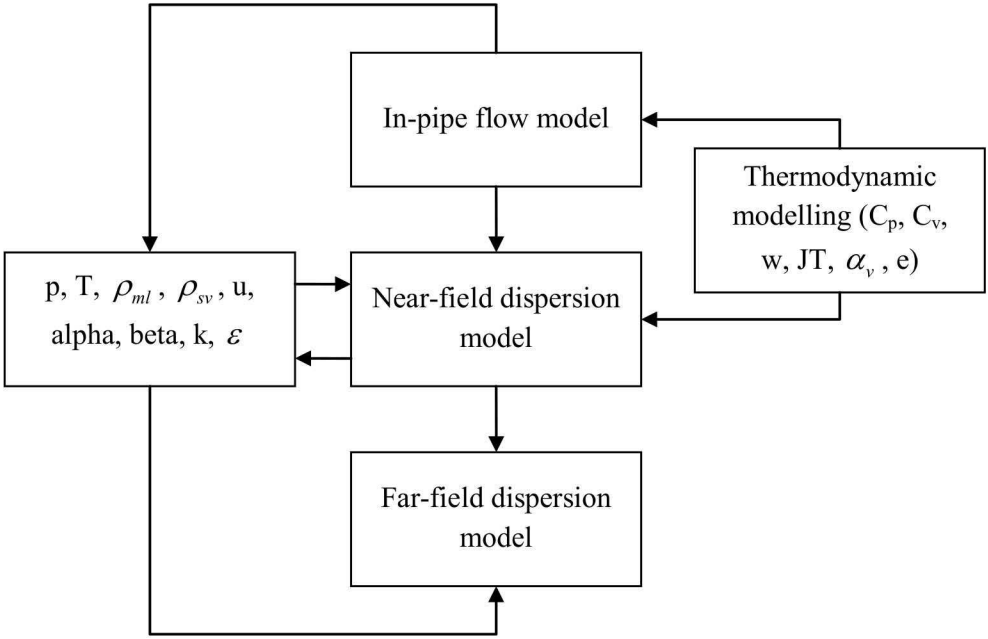
In-pipe flow model
Thermodynamic modelling (C_p, C_v, w, JT, α_v, e)
p, T, ρ_{ml}, ρ_{sv}, u, alpha, beta, k, ε
Near-field dispersion model
Far-field dispersion model

Test Number	Vessel Temperature / K	Ambient Temperature / K	Air Humidity / %	Reservoir Pressure / bar	Nozzle Diameter / mm
2	265.00	272.15	90.0	28.4	6
8	278.15	277.15	95.0	77.0	25

Equation of State	Flow Rate / kg s^{-1}	Density / kg m^{-3}	Pressure Drop from Reservoir / bar	Temperature / K	Liquid Phase Fraction
PR	0.76	1047.11	1.64	253.80	1
SRK	0.66	922.10	1.28	253.97	1
PC-SAFT	0.67	1022.85	1.31	254.21	1
Experiment	0.80 (±0.08)	-	-	265.00	-

Equation of State	Flow Rate / kg s^{-1}	Density / kg m^{-3}	Pressure Drop from Reservoir / bar	Temperature / K	Liquid Phase Fraction
PR	23.93	1064.13	5.76	255.95	1
SRK	20.68	939.64	5.14	256.22	1
Experiment	23.00 (±2.3)	-	≈4.70	-	-

Derivative Thermodynamic Property	Definition
Heat capacity at constant pressure	$C_p = \left.\frac{\partial H}{\partial \mathrm{T}}\right\|_p$
Heat capacity ratio	$\frac{C_p}{C_v} = \frac{C_p}{C_p - \left(C_p - C_v\right)}$
Heat capacity difference	$C_p - C_v = -T\frac{\left(\frac{\partial p}{\partial T}\right)^2}{\frac{\partial p}{\partial v}}$
Speed of sound	$w = \sqrt{\frac{C_p}{C_v}\left(\frac{\partial p}{\partial \rho}\right)_T} = \sqrt{-\frac{C_p}{C_v}\rho^2\left(\frac{\partial p}{\partial v}\right)_T}$
Joule-Thomson coefficient	$JT = \left(\frac{\partial T}{\partial p}\right)_H = \frac{1}{C_p}\left(T\left(\frac{\partial v}{\partial T}\right)_p - v\right)$
Thermal expansion coefficient	$\alpha_v = \frac{1}{v}\left(\frac{\partial v}{\partial T}\right)_p$

Parameter	Value
Total velocity ($m\ s^{-1}$)	70.6
Area (m^2)	62.95
Temperature (K)	194.6
CO_2 mass fraction ($kg\ kg^{-1}$)	0.944
Air mass fraction ($kg\ kg^{-1}$)	0.056
CO_2 gas mass flow rate ($kg\ s^{-1}$)	11486
CO_2 solid mass flow rate ($kg\ s^{-1}$)	8016
Air mass flow rate ($kg\ s^{-1}$)	686
Total mass flow rate ($kg\ s^{-1}$)	20188